Available online at www.sciencedirect.com
SCIENCE DIRECT®
Journal of Computational Physics 208 (2005) 527–569
JOURNAL OF COMPUTATIONAL PHYSICS
www.elsevier.com/locate/jcp

Accurate, efficient and monotonic numerical methods for multi-dimensional compressible flows Part I: Spatial discretization

Kyu Hong Kim, Chongam Kim *

Department of Aerospace Engineering, School of Mechanical and Aerospace Engineering, Seoul National University, Kwanak-Gu, Shilim-Dong, Seoul 151-742, Republic of Korea

Received 16 February 2004; received in revised form 1 February 2005; accepted 28 February 2005
Available online 22 April 2005

Abstract

The present papers deal with numerical methods toward the accurate and efficient computations of multi-dimensional steady/unsteady compressible flows. In Part I, a new spatial discretization technique is introduced to reduce excessive numerical dissipation in a non-flow-aligned grid system. Through the analysis of TVD limiters, a criterion is proposed to predict cell-interface states accurately both in smooth region and in discontinuous region. According to the criterion, a new way of re-evaluating the cell-interface convective flux in AUSM-type methods is developed. The resultant flux reduces numerical dissipation remarkably in multi-dimensional flows. Also, the monotonicity of AUSM-type methods is achieved by modifying the pressure splitting function directly based on the governing equations and the detection of sonic transition point with respect to a cell-interface. It is noted that the newly formulated AUSM-type flux for Multi-dimensional flows, named M-AUSMPW+, possesses many improved properties in term of accuracy, computational efficiency, monotonicity and grid independency.

Through numerous test cases from contact and shock discontinuities, vortex flow, shock wave/boundary-layer interaction to viscous shock tube problems, M-AUSMPW+ proves to be efficient and about twice more accurate than conventional upwind schemes. The three-dimensional implementation of M-AUSMPW+ is expected to provide accuracy and efficiency improvement furthermore.

MSC: 35L65; 65M12; 76K05; 80A32

Keywords: Multi-dimensional flow computations; Advection property; AUSM-type method; M-AUSMPW+; TVD limiting condition; MUSCL

* Corresponding author. Tel.: +82 2 880 1915; fax: +82 2 887 2662.
E-mail address: chongam@snu.ac.kr (C. Kim).

0021-9991/$ - see front matter © 2005 Elsevier Inc. All rights reserved.
doi:10.1016/j.jcp.2005.02.021

1. Introduction

The analysis of more complex flow physics has been required continuously with the development of aerospace industry and it has been also true in the field of computational fluid dynamics. Simultaneously, the more enhanced computing power has been requested for more complex and accurate computations. With the rapid increase of computing power and data storage, three-dimensional unsteady flows can be simulated in a time accurate manner. In addition, the present research trend in CFD emphasizes the multi-disciplinary integrated analysis including fluid dynamics, structure and control. Those requirements, however, are not fully satisfied even with the present computing power. There always seems to be a bottleneck in computational analysis since more complex flow physics is attempted to compute than available computing power. Thus, the fundamental study of numerical schemes which maximizes computational efficiency and numerical accuracy within the given computing power have to be carried out.

Up to now, most popular numerical schemes have been developed based on one-dimensional flow physics. However, due to the essential limitations of this approach in the accurate and efficient calculations of three-dimensional flows, multi-dimensional flow physics needs to be incorporated as much as possible at the design stage of numerical flux functions. In discretizing the governing equations of fluid motions, some degree of numerical errors is inevitably introduced. With the help of many previous studies, a numerical scheme at present can remove errors almost completely in one-dimensional contact or shock discontinuity. It means that the present CFD technique can give very satisfactory results in one-dimensional problems. However, when applied to two- or three-dimensional flows, numerical scheme frequently generates large errors and accuracy becomes deteriorated. In case of three-dimensional computations, it is especially conspicuous. Thus, a denser grid system is necessary, and as a consequence, a large amount of data storage and computational cost are entailed. The blade/vortex interaction of helicopter and the resolution of wake in low Reynolds number flows are some of typical examples. Since computed tip vortex is smeared out very fast compared with real vortex, it is very difficult to examine the tip vortex interaction accurately. As a result, the blade/vortex interaction commonly resorts to vortex modeling method rather than modern CFD. Even though modern CFD techniques are applied, grid system must be sufficiently denser to reduce numerical dissipation. Another example is low Reynolds number flow around small aircrafts such as Micro Air Vehicle or Unmanned Air Vehicles. As the usefulness of small size aircrafts is emphasized in the 21st century, the phenomena of low Reynolds number flows are studied again very much. In low Reynolds number flows around MAV, the lift to drag ratio is generally very low compared to conventional high Reynolds number airplanes. In order to compensate unfavorable aerodynamic characteristics, many studies have been focused on the interaction of unsteady wakes and/or vortices. Lower pressure in vortex core can be used to generate high lift or high lift to drag ratio. For that reason, the strength and velocity of unsteady wakes and/or vortices should be captured accurately.

In analyzing those complex phenomena, accurate and efficient numerical methods reflecting multi-dimensional flow physics are critical. Through the Part I and Part II of the present papers, we describe new numerical approaches which give much better results in multi-dimensional problems. The main focus is to develop numerical methods that eliminate excessive numerical dissipation and upgrade solution accuracy by predicting the physical distribution of flow variables more accurately in multi-space dimensions.

In the first part, a spatial discretization technique is newly developed based on AUSM-type scheme [1]. The core idea of the new scheme is to modify the convective quantity at a cell-interface by reflecting physical and multi-dimensional phenomena. Generally, existing schemes, such as Roe's FDS [2] or AUSM-type schemes [1,3], determine a cell-interface flux from flow quantities obtained at interpolation step. In case of the present method, a criterion to predict more accurate cell-interface state is proposed through the analysis of TVD limiters [4–6], and the convective quantity at a cell-interface is *re-evaluated* according to the criterion. The advantages of the newly determined convective quantity can be examined in two aspects. Firstly, it provides the closer cell-interface approximation of the real physical value than previous approaches.

Secondly, it can eliminate numerical dissipation effectively in a non-aligned grid system. As a result, the present method can improve solution accuracy significantly, especially, in smooth region including contact or slip discontinuity. From extensive numerical analyses and calculations, it is observed that the present method is very useful in multi-dimensional flow computations without compromising computational cost. For that reason, it is coined M-AUSMPW+ which represents AUSMPW+ scheme for multi-dimensional flow calculations.

In the second part, a new limiting method based on multi-dimensional flow phenomena, named MLP (multi-dimensional limiting process), is developed. The outstanding feature of MLP is, among others, the ability to control oscillations in multi-space dimensions. By the help of a multi-dimensional limiting function, MLP shows robust convergence and higher accuracy. As a result, it yields very desirable properties in terms of accuracy, efficiency and robustness compared with other higher order interpolation schemes such as ENO/WENO [7–12], etc. Although, the proposed methods of Part I and Part II are mainly implemented in AUSM-type schemes, they can be applied to other flux functions according to the authors' experience.

The present paper deals with spatial discretization. Following the introduction, the accurate definition of convective quantity at a cell-interface is justified through numerical analyses and the new spatial discretization scheme, named M-AUSMPW+, is developed in Section 2. Next, the characteristics of M-AUSMPW+ in multi-space dimensions are examined in Section 3. In Section 4, numerous test cases are presented to verify the proposed method. Finally, conclusions based on the numerical analyses and computed results are drawn.

2. Key ideas and improvements of baseline scheme

With the continuous advancement of CFD technology and the requirement for the computations of more complex flow physics, computational efficiency becomes a most important factor. At the same time, many studies are focused on parallel computing. It is, however, possible to realize the goal through the advanced design of spatial discretization, interpolation and temporal integration schemes. Thus, by combining both approaches, computational efficiency can be maximized since efficiency improvements due to numerical methods can be independent of parallel computing architecture.

Computational efficiency and solution accuracy can go together because, if a scheme is accurate, physical solution can be obtained on a coarser grid system. In the present paper, the upwind scheme of AUSMPW+ is modified to enhance accuracy without compromising the efficiency of original AUSM-type schemes. The advantage of upwind scheme is that it can represent flow physics properly through the whole Mach number range, i.e., it transfers flow information correctly according to the local feature of wave physics. As a result, upwind scheme can capture discontinuity accurately and robustly. Aside from this, numerical dissipation can be automatically determined through the whole Mach number range. Thus, it is less dependent on user experience. In spite of such merits, upwind scheme seems to provide excessive numerical dissipation in continuous region because it is designed to have optimal numerical dissipation in discontinuity, i.e., it looks more appropriate in discontinuous region.

Therefore, if an upwind scheme contains extra step to distinguish continuous region from discontinuous region, or gently varied region from rapidly varied region, it can provide low dissipative/more accurate results. With regard to this issue, the first objective of the present paper is to introduce a procedure to differentiate continuous region from discontinuous region. The second objective is to improve the shock capturing capability of AUSMPW+ to yield monotonic profile in a steady flow. Even though AUSMPW+ has been developed to remove the overshoot problem of AUSM-type schemes, it is still not perfect since it shows a little overshoot under some condition (see Fig. 6.) and convergence becomes bad in some grid

system [13]. Monotonic shock capturing property reduces grid dependency and improves convergence in all grid systems.

2.1. Baseline scheme: AUSMPW+

AUSMPW+ can be briefly written as follows:

$$\mathbf{F}_{\frac{1}{2}} = \bar{M}_{\mathrm{L}}^{+} c_{\frac{1}{2}} \boldsymbol{\Psi}_{\mathrm{L}} + \bar{M}_{\mathrm{R}}^{-} c_{\frac{1}{2}} \boldsymbol{\Psi}_{\mathrm{R}} + \left(P_{\mathrm{L}}^{+} \boldsymbol{P}_{\mathrm{L}} + P_{\mathrm{R}}^{-} \boldsymbol{P}_{\mathrm{R}}\right), \tag{1}$$

where $\boldsymbol{P} = (0, p, 0)^{\mathrm{T}}$ and $\boldsymbol{\Psi} = (\rho, \rho u, \rho H)^{\mathrm{T}}$. $\boldsymbol{\Psi}$ is constructed from the primitive vector, $\boldsymbol{\Phi} = (\rho, u, p)^{\mathrm{T}}$. The subscripts $\frac{1}{2}$ and (L, R) stand for a cell-interface quantity, and the left and right states across a cell-interface, respectively.

$\bar{M}_{\mathrm{L,R}}^{\pm}$ is the Mach number interpolation function that is written as follows:

$$\text{(i)} \quad m_{\frac{1}{2}} = M_{\mathrm{L}}^{+} + M_{\mathrm{R}}^{-} \geqslant 0, \;\; \bar{M}_{\mathrm{L}}^{+} = M_{\mathrm{L}}^{+} + M_{\mathrm{R}}^{-} \cdot [(1-w)\cdot(1+f_{\mathrm{R}}) - f_{\mathrm{L}}], \;\; \bar{M}_{\mathrm{R}}^{-} = M_{\mathrm{R}}^{-} \cdot w \cdot (1+f_{\mathrm{R}}), \tag{2a}$$

$$\text{(ii)} \quad m_{\frac{1}{2}} < 0, \;\; \bar{M}_{\mathrm{L}}^{+} = M_{\mathrm{L}}^{+} \cdot w \cdot (1+f_{\mathrm{L}}), \;\; \bar{M}_{\mathrm{R}}^{-} = M_{\mathrm{R}}^{-} + M_{\mathrm{L}}^{+} \cdot [(1-w)\cdot(1+f_{\mathrm{L}}) - f_{\mathrm{R}})], \tag{2b}$$

where the function f and w are pressure and Mach number based weighting functions.

Mach number splitting function $M_{\mathrm{L,R}}^{\pm}$ are given by

$$M_{\mathrm{L,R}}^{\pm} = \begin{cases} \pm\frac{1}{4}(M_{\mathrm{L,R}} \pm 1)^2, & |M_{\mathrm{L,R}}| \leqslant 1, \\ \frac{1}{2}(M_{\mathrm{L,R}} \pm |M_{\mathrm{L,R}}|), & |M_{\mathrm{L,R}}| > 1, \end{cases} \tag{3}$$

where $M_{\mathrm{L,R}} = U_{\mathrm{L,R}}/c_{\frac{1}{2}}$ and $c_{\frac{1}{2}}$ is defined as follows:

$$\text{(i)} \quad \tfrac{1}{2}(U_{\mathrm{L}} + U_{\mathrm{R}}) \geqslant 0: \quad c_{\frac{1}{2}} = c_s^2 / \max(|U_{\mathrm{L}}|, c_s),$$

$$\text{(ii)} \quad \tfrac{1}{2}(U_{\mathrm{L}} + U_{\mathrm{R}}) < 0: \quad c_{\frac{1}{2}} = c_s^2 / \max(|U_{\mathrm{R}}|, c_s).$$

Here, $c_s = \sqrt{2(\gamma-1)/(\gamma+1)H_{\mathrm{normal}}}$ and $H_{\mathrm{normal}} = \min(H_{\mathrm{L}} - 0.5 \times V_{\mathrm{L}}^2, H_{\mathrm{R}} - 0.5 \times V_{\mathrm{R}}^2)$. V is the transversal velocity component to a cell-interface. And the pressure splitting function $P_{\mathrm{L,R}}^{\pm}$ are given as follows:

$$P_{\mathrm{L,R}}^{\pm} = \begin{cases} \frac{1}{4}(M_{\mathrm{L,R}} \pm 1)^2(2 \mp M_{\mathrm{L,R}}), & |M_{\mathrm{L,R}}| \leqslant 1, \\ \frac{1}{2}(1 \pm \mathrm{sign}(M_{\mathrm{L,R}})), & |M_{\mathrm{L,R}}| > 1. \end{cases} \tag{4}$$

AUSMPW+ has been developed to improve the monotonic characteristics of AUSM-type schemes. AUSM-type schemes generally show a good performance in terms of accuracy, robustness and efficiency, which is essential especially in hypersonic and reactive flow simulations. However, the advection characteristic of AUSM-type schemes should be treated carefully because it is the direct cause of numerical overshoots or oscillations. By controlling the advection characteristic with the weighting functions f and w, AUSMPW+ has successfully removed the overshoot phenomena without compromising efficiency and accuracy. Details can be found in [1].

2.2. Method to treat continuous region

AUSM-type schemes define the Mach number at a cell-interface and transfer the flux quantity according to its sign, which is called the advection property. The convective flux of AUSM-type schemes is written as follows:

$$\mathbf{F}_{\frac{1}{2}} = m_{\frac{1}{2}} c_{\frac{1}{2}} \boldsymbol{\Psi}_{\mathrm{L\,or\,R}}, \tag{5}$$

where $m_{\frac{1}{2}}$ is the cell-interface Mach number and $\boldsymbol{\Psi}$ is the transferred quantity vector. If a flux function can recognize the difference between the region of discontinuity and continuity more clearly, it can give more accurate results. As a flexible way to clarify the two regions, the following flux form is considered:

$$\mathbf{F}_{\frac{1}{2}} = m_{\frac{1}{2}} c_{\frac{1}{2}} \boldsymbol{\Psi}_{\mathrm{L\,or\,R},\frac{1}{2}}, \tag{6}$$

where the subscript $\frac{1}{2}$ represents the quantity defined at a cell-interface. Simply stated, the fundamental difference from previous AUSM-type schemes is to modify the convective quantity at a cell-interface appropriately in discontinuous and continuous regions. The convective quantity, $\boldsymbol{\Psi}_{\mathrm{L,R},\frac{1}{2}}$, is determined to satisfy the following requirements:

r1. In order to increase accuracy in continuous region, the convective quantity should be able to distinguish the region of continuity from discontinuity, or expressing it more mildly, gently varied region from rapidly varied region.
r2. The convective quantity should satisfy the monotonic condition.
r3. The convective quantity should maintain the upwind characteristic in supersonic flow.

Requirement 1 is the major objective of the present paper. Requirement 2 is necessary to prevent oscillatory behaviors across discontinuities. The final requirement is essential to represent physical phenomena correctly in supersonic flow.

2.2.1. Requirement 1

Since the transferred quantity vector $\boldsymbol{\Psi} = (\rho, \rho u, \rho H)^{\mathrm{T}}$ is calculated by primitive variable vector $\boldsymbol{\Phi} = (\rho, u, p)^{\mathrm{T}}$, re-evaluating procedure is explained using primitive variable vector.

Firstly, the characteristics of continuous and discontinuous regions are examined to establish the criterion that divides the two regions. The convective quantity at a cell-interface is then re-evaluated according to the criterion. The ideal case would be that the Mach number and convective quantity at a cell-interface are exactly the same as the physical values. Alternatively, if we can find out $\boldsymbol{\Phi}_{\mathrm{L,R},\frac{1}{2}}$ which is closer to the real physical value than $\boldsymbol{\Phi}_{\mathrm{L\,or\,R}}$, Eq. (6) will be very effective.

In order to obtain information on the distribution of the physical value, TVD interpolation [4,5] is analyzed. All the vector notations in Part I and Part II are introduced for compact expression. Thus, in actual implementation, they should be applied component by component. Through interpolation step, cell-interface quantities are prepared as:

$$\boldsymbol{\Phi}_{\mathrm{L}} = \bar{\boldsymbol{\Phi}}_i + 0.5\Delta\boldsymbol{\Phi}|_i = \bar{\boldsymbol{\Phi}}_i + 0.5\phi(r_{\mathrm{L}})\Delta\boldsymbol{\Phi}_{i-\frac{1}{2}}, \tag{7a}$$

$$\boldsymbol{\Phi}_{\mathrm{R}} = \bar{\boldsymbol{\Phi}}_{i+1} - 0.5\Delta\boldsymbol{\Phi}|_{i+1} = \bar{\boldsymbol{\Phi}}_{i+1} - 0.5\phi(r_{\mathrm{R}})\Delta\boldsymbol{\Phi}_{i+\frac{3}{2}}, \tag{7b}$$

where ϕ is TVD limiter and $r_{\mathrm{L}} = \Delta\boldsymbol{\Phi}_{i+\frac{1}{2}}/\Delta\boldsymbol{\Phi}_{i-\frac{1}{2}}$, $r_{\mathrm{R}} = \Delta\boldsymbol{\Phi}_{i+\frac{1}{2}}/\Delta\boldsymbol{\Phi}_{i+\frac{3}{2}}$. And variation at each cell-interface is defined as follows:

$$\Delta\boldsymbol{\Phi}_{i-\frac{1}{2}} = \bar{\boldsymbol{\Phi}}_i - \bar{\boldsymbol{\Phi}}_{i-1}, \quad \Delta\boldsymbol{\Phi}_{i+\frac{1}{2}} = \bar{\boldsymbol{\Phi}}_{i+1} - \bar{\boldsymbol{\Phi}}_i, \quad \Delta\boldsymbol{\Phi}_{i+\frac{3}{2}} = \bar{\boldsymbol{\Phi}}_{i+2} - \bar{\boldsymbol{\Phi}}_{i+1}, \tag{8}$$

where the bar means a cell averaged value.

Except for the region of local extrema, the accuracy of TVD interpolation (Eq. (7)) can be expressed by Taylor expansion with respect to the location of $i + \frac{1}{2}$ as:

$$\boldsymbol{\Phi}_{\mathrm{L,R}} = \boldsymbol{\Phi}_{i+\frac{1}{2}} + \Delta x^2 \boldsymbol{\Phi}'' \left[\frac{1}{2}\phi'(1) - \frac{1}{3}\right] + \mathrm{O}(\Delta x^3), \tag{9a}$$

$$\boldsymbol{\Phi}_{\mathrm{L,R},\frac{1}{2}} = 0.5(\boldsymbol{\Phi}_{\mathrm{L}} + \boldsymbol{\Phi}_{\mathrm{R}}) = \boldsymbol{\Phi}_{i+\frac{1}{2}} + \frac{\Delta x^2}{2}\boldsymbol{\Phi}''\left[\left(\frac{1}{2}\phi'(1) - \frac{1}{3}\right)_{\mathrm{L}} + \left(\frac{1}{2}\phi'(1) - \frac{1}{3}\right)_{\mathrm{R}}\right] + \mathrm{O}(\Delta x^3). \tag{9b}$$

The leading error term is second order and becomes third order accurate if $\phi'(1) = \frac{2}{3}$. Let us consider the case that physical property is represented as $\boldsymbol{\Phi}_{\mathrm{real}}$ and it satisfies the concave condition of $\partial\boldsymbol{\Phi}_{\mathrm{real}}/\partial x > 0$ and $\partial^2\boldsymbol{\Phi}_{\mathrm{real}}/\partial x^2 > 0$ as in Fig. 1, where $r_{\mathrm{L}} > 1$ and $0 < r_{\mathrm{R}} < \frac{1}{r_{\mathrm{L}}}$.

At first, minmod limiter is considered as the most diffusive second order TVD interpolation. It chooses the smallest variation of the two candidates as

$$\phi(r) = \max(0, \min(r, 1)). \tag{10}$$

When $r_{\mathrm{L}} > 1$ and $0 < r_{\mathrm{R}} < \frac{1}{r_{\mathrm{L}}}$, it gives:

$$\boldsymbol{\Phi}_{\mathrm{L,min\ mod}} = \boldsymbol{\Phi}_{\mathrm{real},i+\frac{1}{2}} - \frac{\Delta x^2}{3}\boldsymbol{\Phi}'' + \mathrm{O}(\Delta x^3), \tag{11a}$$

$$\boldsymbol{\Phi}_{\mathrm{R,min\ mod}} = \boldsymbol{\Phi}_{\mathrm{real},i+\frac{1}{2}} + \frac{\Delta x^2}{6}\boldsymbol{\Phi}'' + \mathrm{O}(\Delta x^3), \tag{11b}$$

where the subscription of 'real' means the physical value. Assuming Δx is sufficiently small and neglecting the higher order term of $\mathrm{O}(\Delta x^3)$

$$\bar{\boldsymbol{\Phi}}_i < \boldsymbol{\Phi}_{\mathrm{L,min\ mod}} < \boldsymbol{\Phi}_{\mathrm{real},i+\frac{1}{2}} < \boldsymbol{\Phi}_{\mathrm{R,min\ mod}} < \bar{\boldsymbol{\Phi}}_{i+1}. \tag{12}$$

Fig. 2 shows the relation between the minmod interpolation value and the physical value. Now, let us define the transferred quantity as $\boldsymbol{\Phi}_{\mathrm{L},\frac{1}{2}} = \boldsymbol{\Phi}_{\mathrm{R},\frac{1}{2}} = 0.5(\boldsymbol{\Phi}_{\mathrm{L,min\ mod}} + \boldsymbol{\Phi}_{\mathrm{R,min\ mod}})$. Then

$$\boldsymbol{\Phi}_{\mathrm{L,R},\frac{1}{2}} = \boldsymbol{\Phi}_{\mathrm{real},i+\frac{1}{2}} - \frac{\Delta x^2}{12}\boldsymbol{\Phi}'' + \mathrm{O}(\Delta x^3). \tag{13}$$

Eq. (13) shows that the averaged value $\boldsymbol{\Phi}_{\mathrm{L,R},\frac{1}{2}}$ is still 2nd-order accurate. However, the error is reduced to one-fourth compared to $\boldsymbol{\Phi}_{\mathrm{L,min\ mod}}$ and is smaller than $\boldsymbol{\Phi}_{\mathrm{L,R,min\ mod}}$. Thus, the re-evaluated convective quantity, $\boldsymbol{\Phi}_{\mathrm{L,R},\frac{1}{2}} = 0.5(\boldsymbol{\Phi}_{\mathrm{L,min\ mod}} + \boldsymbol{\Phi}_{\mathrm{R,min\ mod}})$ is always closer to $\boldsymbol{\Phi}_{\mathrm{real},i+\frac{1}{2}}$ than $\boldsymbol{\Phi}_{\mathrm{L,min\ mod}}$ and $\boldsymbol{\Phi}_{\mathrm{R,min\ mod}}$.

Next, discontinuous or rapidly varied region is examined. Discontinuous region is thoroughly different in its nature from smooth region. Variation in discontinuous region should be determined in a way that it makes the largest variation or the steepest slope possible within monotonic constraint because the derivative of $\partial\boldsymbol{\Phi}_{\mathrm{real}}/\partial x$ at discontinuity is infinite mathematically. In this case, the variation of $|\boldsymbol{\Phi}_{\mathrm{L},\frac{1}{2}} - \bar{\boldsymbol{\Phi}}_i|$ and $|\boldsymbol{\Phi}_{\mathrm{R},\frac{1}{2}} - \bar{\boldsymbol{\Phi}}_{i+1}|$ is always greater than the variation by minmod, $|\boldsymbol{\Phi}_{\mathrm{L,min\ mod}} - \bar{\boldsymbol{\Phi}}_i|$ and $|\boldsymbol{\Phi}_{\mathrm{R,min\ mod}} - \bar{\boldsymbol{\Phi}}_{i+1}|$, respectively.

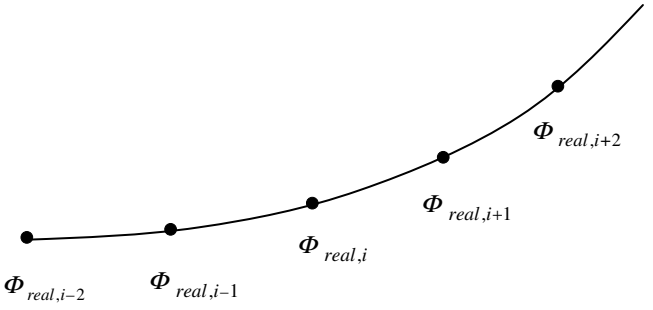

Fig. 1. Physical distribution of $\partial\boldsymbol{\Phi}_{\mathrm{real}}/\partial x > 0$ and $\partial^2\boldsymbol{\Phi}_{\mathrm{real}}/\partial x^2 > 0$.

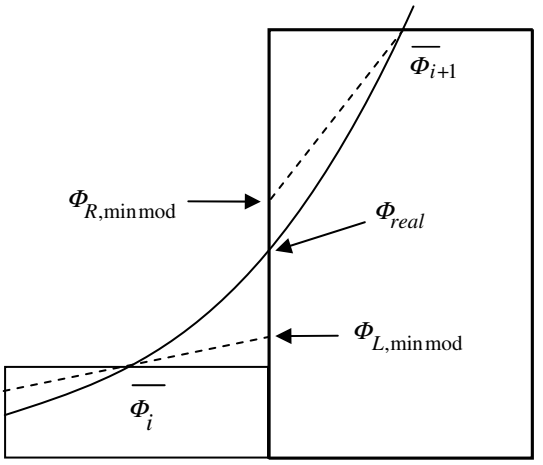

Fig. 2. Physical distribution and numerical approximation by minmod limiter.

Thus, it is expected that solution is always improved both in continuous and in discontinuous region if the convective quantity is re-evaluated as $0.5(\boldsymbol{\Phi}_{\text{L,min mod}} + \boldsymbol{\Phi}_{\text{R,min mod}})$.

Secondly, as the most compressive second order TVD limiter, superbee limiter is considered. It chooses the steeper variation of the two candidates as

$$\phi(r) = \max(0, \min(2r, 1), \min(r, 2)). \tag{14}$$

From Eq. (9), we have:

$$\boldsymbol{\Phi}_{\text{L,superbee}} = \boldsymbol{\Phi}_{\text{real},i+\frac{1}{2}} + \frac{\Delta x^2}{6}\boldsymbol{\Phi}'' + \mathrm{O}(\Delta x^3), \tag{15a}$$

$$\boldsymbol{\Phi}_{\text{R,superbee}} = \boldsymbol{\Phi}_{\text{real},i+\frac{1}{2}} - \frac{\Delta x^2}{3}\boldsymbol{\Phi}'' + \mathrm{O}(\Delta x^3). \tag{15b}$$

Similar to the case of minmod, we have Eq. (16) from Eq. (15)

$$\bar{\boldsymbol{\Phi}}_i < \boldsymbol{\Phi}_{\text{R,superbee}} < \boldsymbol{\Phi}_{\text{real},i+\frac{1}{2}} < \boldsymbol{\Phi}_{\text{L,superbee}} < \bar{\boldsymbol{\Phi}}_{i+1}. \tag{16}$$

Fig. 3 shows the relation between superbee interpolated value and the physical value. And, the re-evaluated convective quantity is given by

$$\boldsymbol{\Phi}_{\text{L,R},\frac{1}{2}} = \boldsymbol{\Phi}_{\text{real},i+\frac{1}{2}} - \frac{\Delta x^2}{12}\boldsymbol{\Phi}'' + \mathrm{O}(\Delta x^3). \tag{17}$$

Again, the error is reduced to one-fourth compared to $\boldsymbol{\Phi}_{\text{R,superbee}}$ or its magnitude is smaller than that of $\boldsymbol{\Phi}_{\text{L,R,superbee}}$. Thus, the re-evaluated convective quantity, $\boldsymbol{\Phi}_{\text{L,R},\frac{1}{2}} = 0.5(\boldsymbol{\Phi}_{\text{L,superbee}} + \boldsymbol{\Phi}_{\text{R,superbee}})$ predict a better approximation than the original interpolated values in smooth region. In discontinuous region, $\boldsymbol{\Phi}_{\text{L,superbee}}$ is always larger than $\boldsymbol{\Phi}_{\text{R,superbee}}$ as in Eq. (16) and thus $|\boldsymbol{\Phi}_{\text{L},\frac{1}{2}} - \bar{\boldsymbol{\Phi}}_i|$ is always less than $|\boldsymbol{\Phi}_{\text{L,superbee}} - \bar{\boldsymbol{\Phi}}_i|$. As a result, different from minmod limiter, accuracy is not improved with the re-evaluated quantity. It gives more numerical viscosity.

Based on the previous analysis, the case of $\partial\boldsymbol{\Phi}_{\text{real}}/\partial x > 0$ and $\partial^2\boldsymbol{\Phi}_{\text{real}}/\partial x^2 > 0$ can be summarized as follows. In smooth region, the re-evaluation of $\boldsymbol{\Phi}_{\text{L,R},\frac{1}{2}} = 0.5(\boldsymbol{\Phi}_{\text{L}} + \boldsymbol{\Phi}_{\text{R}})$ is always expected to yield more accurate results than minmod and superbee limiters. In discontinuous region, accuracy would be enhanced only in minmod case.

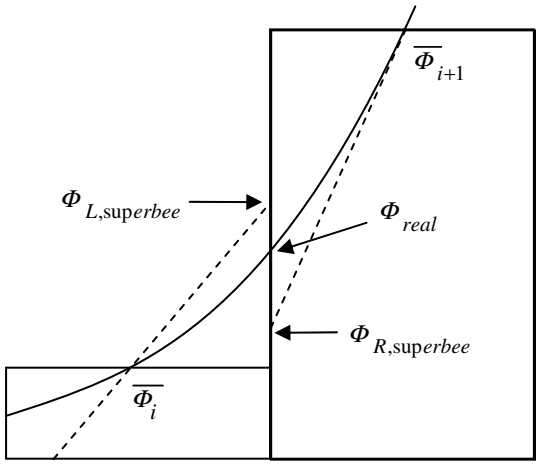

Fig. 3. Physical distribution and numerical approximation by superbee limiter.

Lastly, let us consider differentiable and symmetric 2nd order TVD limiters such as van Leer limiter. Then, from $\phi'(1) = 0.5$ and Eq. (9b), the leading error of the averaged value is the same as Eq. (9a). However, as will be explained in Proposition (Eq. (18)) and Section 3.1.2, the proposed re-evaluation always selects steeper variation and as a result numerical viscosity is reduced.

When the distribution of $\boldsymbol{\Phi}_{\mathrm{real}}$ is different, such as, $\partial\boldsymbol{\Phi}_{\mathrm{real}}/\partial x < 0$ and $\partial^2\boldsymbol{\Phi}_{\mathrm{real}}/\partial x^2 > 0$, r_{L} is between 0 and 1 and r_{R} is between 1 and $1/r_{\mathrm{L}}$. Similarly, in case of $\partial\boldsymbol{\Phi}_{\mathrm{real}}/\partial x > 0$ and $\partial^2\boldsymbol{\Phi}_{\mathrm{real}}/\partial x^2 < 0$, $r_{\mathrm{L,R}}$ is $0 < r_{\mathrm{L}} < 1$ and $1 < r_{\mathrm{R}} < \frac{1}{r_{\mathrm{L}}}$. In case of $\partial\boldsymbol{\Phi}_{\mathrm{real}}/\partial x < 0$ and $\partial^2\boldsymbol{\Phi}_{\mathrm{real}}/\partial x^2 < 0$, $r_{\mathrm{L,R}}$ is $r_{\mathrm{L}} > 1$ and $0 < r_{\mathrm{R}} < \frac{1}{r_{\mathrm{L}}}$. Through the similar analysis, it can be shown that all other cases yield the same results.

When there is an inflection point ($r_{\mathrm{L}}, r_{\mathrm{R}} > 1$ or $0 < r_{\mathrm{L}}, r_{\mathrm{R}} < 1$), the leading error of the averaged value in Eq. (9b) is the same as Eq. (9a) because of $\phi'_{\mathrm{L}}(1) = \phi'_{\mathrm{R}}(1)$. Lastly, overall accuracy becomes first order at local extrema. But the averaged value is still effective because the leading error term after re-evaluation is reduced by half.

Eqs. (12) and (16) reveal an important property which should be fully exploited in evaluating limited variations. The derivative of $\partial\boldsymbol{\Phi}_{\mathrm{real}}/\partial x$ at discontinuity is infinite mathematically. Thus, when variations are estimated accordingly, the condition of $\boldsymbol{\Phi}_{\mathrm{R}} < \boldsymbol{\Phi}_{\mathrm{L}}$ (see Eq. (7)) can be readily derived as in superbee limiter, which is quite reasonable in rapidly varied region. However, if the same interpolated values are applied to gently varied region, computations is likely to be unstable due to excessive variation, or too much compression of $\boldsymbol{\Phi}_{\mathrm{L\ or\ R}}$. The computation of vortex flow in Section 4 would be a good example. The weak point of minmod and superbee limiters is due to their consistent numerical behaviors regardless of the nature of the real physical distribution.

Therefore, based on the previous analysis on TVD limiters, we identify rapidly varied region or discontinuous region by the condition of $\bar{\boldsymbol{\Phi}}_i < \boldsymbol{\Phi}_{\mathrm{R}} < \boldsymbol{\Phi}_{\mathrm{L}} < \bar{\boldsymbol{\Phi}}_{i+1}$. And, the criterion to distinguish gently varied region from rapidly varied region is proposed as follows.

Gently varied region:

$$\bar{\boldsymbol{\Phi}}_i < \boldsymbol{\Phi}_{\mathrm{L}} < \boldsymbol{\Phi}_{\mathrm{R}} < \bar{\boldsymbol{\Phi}}_{i+1}, \tag{18a}$$

Rapidly varied region:

$$\bar{\boldsymbol{\Phi}}_i < \boldsymbol{\Phi}_{\mathrm{R}} < \boldsymbol{\Phi}_{\mathrm{L}} < \bar{\boldsymbol{\Phi}}_{i+1}. \tag{18b}$$

Responding to the requirement $r1$ mentioned in this section, the following criterion is proposed.

Proposition. *If the interpolated value of $\Phi_{L\ and\ R}$ satisfies the condition of Eq. (18a), the physical state at a cell-interface is considered to be in continuous region and the convective property at a cell-interface is modified as $\boldsymbol{\Phi}_{L,\frac{1}{2}} = \boldsymbol{\Phi}_{R,\frac{1}{2}} = 0.5(\boldsymbol{\Phi}_L + \boldsymbol{\Phi}_R)$. If $\Phi_{L\ and\ R}$ satisfies the condition of Eq. (18b), it is considered to in discontinuous region and the interpolated value is not re-evaluated.*

Then, the re-evaluated value, $\boldsymbol{\Phi}_{\mathrm{L,R},\frac{1}{2}}$ is closer to the physical value than the original interpolated value.

Eq. (18a) can be rewritten as follows:

$$\bar{\boldsymbol{\Phi}}_i < \boldsymbol{\Phi}_{\mathrm{L}} < 0.5(\boldsymbol{\Phi}_{\mathrm{L}} + \boldsymbol{\Phi}_{\mathrm{R}}) < \boldsymbol{\Phi}_{\mathrm{R}} < \bar{\boldsymbol{\Phi}}_{i+1}. \tag{19a}$$

Or more generally

$$\left|\boldsymbol{\Phi}_{\mathrm{L}} - \bar{\boldsymbol{\Phi}}_i\right| \leqslant \left|0.5(\boldsymbol{\Phi}_{\mathrm{L}} + \boldsymbol{\Phi}_{\mathrm{R}}) - \bar{\boldsymbol{\Phi}}_i\right| \quad \text{or} \quad (0.5(\boldsymbol{\Phi}_{\mathrm{L}} + \boldsymbol{\Phi}_{\mathrm{R}}) - \boldsymbol{\Phi}_{\mathrm{L}})\left(\boldsymbol{\Phi}_{\mathrm{L,superbee}} - \boldsymbol{\Phi}_{\mathrm{L}}\right) \geqslant 0. \tag{19b}$$

Here, $\boldsymbol{\Phi}_{\mathrm{L}}$ lies between $\boldsymbol{\Phi}_{\mathrm{L,min\ mod}}$ and $\boldsymbol{\Phi}_{\mathrm{L,superbee}}$, and the convective quantity is determined as follows.

In gently varied region, $(0.5(\boldsymbol{\Phi}_{\mathrm{L}} + \boldsymbol{\Phi}_{\mathrm{R}}) - \boldsymbol{\Phi}_{\mathrm{L}})(\boldsymbol{\Phi}_{\mathrm{L,superbee}} - \boldsymbol{\Phi}_{\mathrm{L}}) = 0.5(\boldsymbol{\Phi}_{\mathrm{R}} - \boldsymbol{\Phi}_{\mathrm{L}})(\boldsymbol{\Phi}_{\mathrm{L,superbee}} - \boldsymbol{\Phi}_{\mathrm{L}}) \geqslant 0$

$$\boldsymbol{\Phi}_{\mathrm{L},i+\frac{1}{2}} = 0.5(\boldsymbol{\Phi}_{\mathrm{L}} + \boldsymbol{\Phi}_{\mathrm{R}}). \tag{20a}$$

In rapidly varied region, $0.5(\boldsymbol{\Phi}_{\mathrm{R}} - \boldsymbol{\Phi}_{\mathrm{L}})(\boldsymbol{\Phi}_{\mathrm{L,superbee}} - \boldsymbol{\Phi}_{\mathrm{L}}) < 0$

$$\boldsymbol{\Phi}_{\mathrm{L},i+\frac{1}{2}} = \boldsymbol{\Phi}_{\mathrm{L}}. \tag{20b}$$

As a consequence, $\boldsymbol{\Phi}_{\mathrm{L},i+\frac{1}{2}}$ always gives a larger variation, i.e., less numerical dissipation than the original value and thus accuracy is enhanced.

Now, we also consider the case of general pth order interpolation. The left and right interpolated values have the same magnitude with the opposite sign for the leading error term:

$$\boldsymbol{\Phi}_{\mathrm{L}} = \boldsymbol{\Phi}_{\mathrm{real},i+\frac{1}{2}} + c\frac{\partial^p \boldsymbol{\Phi}}{\partial x^p} + \mathrm{O}\left(\Delta x^{p+1}\right), \tag{21a}$$

$$\boldsymbol{\Phi}_{\mathrm{R}} = \boldsymbol{\Phi}_{\mathrm{real},i+\frac{1}{2}} - c\frac{\partial^p \boldsymbol{\Phi}}{\partial x^p} + \mathrm{O}\left(\Delta x^{p+1}\right), \tag{21b}$$

where p is an odd number.

Then, the averaged value of $\boldsymbol{\Phi}_{\mathrm{L},\frac{1}{2}} = \boldsymbol{\Phi}_{\mathrm{R},\frac{1}{2}} = 0.5(\boldsymbol{\Phi}_{\mathrm{L}} + \boldsymbol{\Phi}_{\mathrm{R}})$ has the $(p+1)$th order leading error term, i.e., accuracy is increased by one order of magnitude

$$\boldsymbol{\Phi}_{\mathrm{L},\frac{1}{2}} = \boldsymbol{\Phi}_{\mathrm{R},\frac{1}{2}} = 0.5(\boldsymbol{\Phi}_{\mathrm{L}} + \boldsymbol{\Phi}_{\mathrm{R}}) = \boldsymbol{\Phi}_{\mathrm{real},i+\frac{1}{2}} + \mathrm{O}\left(\Delta x^{p+1}\right). \tag{22}$$

In general, most pth order interpolation schemes maintain the accuracy level of Eq. (21) in gently varied region. Thus, when the re-evaluated form of Eq. (22) adopts 3rd or 5th order interpolation schemes, the results in the region of $\bar{\boldsymbol{\Phi}}_i < \boldsymbol{\Phi}_{\mathrm{L}} < \boldsymbol{\Phi}_{\mathrm{R}} < \bar{\boldsymbol{\Phi}}_{i+1}$ is much more improved than 2nd order case. This will be shown in Part II.

2.2.2. Requirement 2

With regard to the requirement $r2$ for the monotonic distribution, the re-evaluated value at a cell-interface should satisfy the following constraint:

$$\min\left(\boldsymbol{\Phi}_{\mathrm{L,min\,mod}}, \boldsymbol{\Phi}_{\mathrm{L,superbee}}\right) \leqslant \boldsymbol{\Phi}_{\mathrm{L},\frac{1}{2}} \leqslant \max\left(\boldsymbol{\Phi}_{\mathrm{L,min\,mod}}, \boldsymbol{\Phi}_{\mathrm{L,superbee}}\right). \tag{23}$$

Many researches have been conducted to preserve accuracy at local extrema by introducing TVB [14], ENO [7], MP schemes [15], or extended TVD approaches [10,16]. Their results show that smooth extremum can be treated successfully with less restrictive condition. For the purpose of robust convergence, however, the re-evaluation procedure adopts TVD. Eq. (23) can be written as

$$\bar{\boldsymbol{\Phi}}_i < \boldsymbol{\Phi}_{\mathrm{L,min\ mod}} < \boldsymbol{\Phi}_{\mathrm{L},\frac{1}{2}} = 0.5(\boldsymbol{\Phi}_{\mathrm{L}} + \boldsymbol{\Phi}_{\mathrm{R}}) < \boldsymbol{\Phi}_{\mathrm{L,superbee}} < \bar{\boldsymbol{\Phi}}_{i+1}. \tag{24}$$

After applying the monotonic condition to Eq. (20), we have

$$\boldsymbol{\Phi}_{\mathrm{L},\frac{1}{2}} = \boldsymbol{\Phi}_{\mathrm{L}} + \mathrm{sign}\left(\boldsymbol{\Phi}_{\mathrm{L,superbee}} - \boldsymbol{\Phi}_{\mathrm{L}}\right) \min\left(|0.5(\boldsymbol{\Phi}_{\mathrm{R}} - \boldsymbol{\Phi}_{\mathrm{L}})|, \left|\boldsymbol{\Phi}_{\mathrm{L,superbee}} - \boldsymbol{\Phi}_{\mathrm{L}}\right|\right) \tag{25a}$$

if $(\boldsymbol{\Phi}_{\mathrm{R}} - \boldsymbol{\Phi}_{\mathrm{L}})(\boldsymbol{\Phi}_{\mathrm{L,superbee}} - \boldsymbol{\Phi}_{\mathrm{L}}) \geqslant 0$.

$$\boldsymbol{\Phi}_{\mathrm{L},\frac{1}{2}} = \boldsymbol{\Phi}_{\mathrm{L}} \tag{25b}$$

if $(\boldsymbol{\Phi}_{\mathrm{R}} - \boldsymbol{\Phi}_{\mathrm{L}})(\boldsymbol{\Phi}_{\mathrm{L,superbee}} - \boldsymbol{\Phi}_{\mathrm{L}}) < 0$.

In brief, the property at a cell-interface can be rewritten as follows:

$$\boldsymbol{\Phi}_{\mathrm{L},\frac{1}{2}} = \boldsymbol{\Phi}_{\mathrm{L}} + \frac{\max\left[0, (\boldsymbol{\Phi}_{\mathrm{R}} - \boldsymbol{\Phi}_{\mathrm{L}})\left(\boldsymbol{\Phi}_{\mathrm{L,superbee}} - \boldsymbol{\Phi}_{\mathrm{L}}\right)\right]}{(\boldsymbol{\Phi}_{\mathrm{R}} - \boldsymbol{\Phi}_{\mathrm{L}})\left|\boldsymbol{\Phi}_{\mathrm{L,superbee}} - \boldsymbol{\Phi}_{\mathrm{L}}\right|} \min\left[\frac{|\boldsymbol{\Phi}_{\mathrm{R}} - \boldsymbol{\Phi}_{\mathrm{L}}|}{2}, \left|\boldsymbol{\Phi}_{\mathrm{L,superbee}} - \boldsymbol{\Phi}_{\mathrm{L}}\right|\right], \tag{26a}$$

$$\boldsymbol{\Phi}_{\mathrm{R},\frac{1}{2}} = \boldsymbol{\Phi}_{\mathrm{R}} + \frac{\max\left[0, (\boldsymbol{\Phi}_{\mathrm{L}} - \boldsymbol{\Phi}_{\mathrm{R}})\left(\boldsymbol{\Phi}_{\mathrm{R,superbee}} - \boldsymbol{\Phi}_{\mathrm{R}}\right)\right]}{(\boldsymbol{\Phi}_{\mathrm{L}} - \boldsymbol{\Phi}_{\mathrm{R}})\left|\boldsymbol{\Phi}_{\mathrm{R,superbee}} - \boldsymbol{\Phi}_{\mathrm{R}}\right|} \min\left[\frac{|\boldsymbol{\Phi}_{\mathrm{L}} - \boldsymbol{\Phi}_{\mathrm{R}}|}{2}, \left|\boldsymbol{\Phi}_{\mathrm{R,superbee}} - \boldsymbol{\Phi}_{\mathrm{R}}\right|\right]. \tag{26b}$$

2.2.3. Requirement 3

Eq. (26) should exhibit complete upwinding in supersonic region. However, the form of $\boldsymbol{\Phi}_{\frac{1}{2}} = 0.5(\boldsymbol{\Phi}_{\mathrm{L}} + \boldsymbol{\Phi}_{\mathrm{R}})$ is not correct in supersonic flows although it is appropriate in subsonic flows. This suggests that $\boldsymbol{\Phi}_{\frac{1}{2}}$ should be determined after a cell-interface state is identified whether it belongs to subsonic or supersonic region. A simple quadratic function is introduced for that purpose, and the convective quantity at a cell-interface is finally formulated as follows:

$$\boldsymbol{\Phi}_{\mathrm{L},\frac{1}{2}} = \boldsymbol{\Phi}_{\mathrm{L}} + \frac{\max\left[0, (\boldsymbol{\Phi}_{\mathrm{R}} - \boldsymbol{\Phi}_{\mathrm{L}})\left(\boldsymbol{\Phi}_{\mathrm{L,superbee}} - \boldsymbol{\Phi}_{\mathrm{L}}\right)\right]}{(\boldsymbol{\Phi}_{\mathrm{R}} - \boldsymbol{\Phi}_{\mathrm{L}})\left|\boldsymbol{\Phi}_{\mathrm{L,superbee}} - \boldsymbol{\Phi}_{\mathrm{L}}\right|} \min\left[a\frac{|\boldsymbol{\Phi}_{\mathrm{R}} - \boldsymbol{\Phi}_{\mathrm{L}}|}{2}, \left|\boldsymbol{\Phi}_{\mathrm{L,superbee}} - \boldsymbol{\Phi}_{\mathrm{L}}\right|\right], \tag{27a}$$

$$\boldsymbol{\Phi}_{\mathrm{R},\frac{1}{2}} = \boldsymbol{\Phi}_{\mathrm{R}} + \frac{\max\left[0, (\boldsymbol{\Phi}_{\mathrm{L}} - \boldsymbol{\Phi}_{\mathrm{R}})\left(\boldsymbol{\Phi}_{\mathrm{R,superbee}} - \boldsymbol{\Phi}_{\mathrm{R}}\right)\right]}{(\boldsymbol{\Phi}_{\mathrm{L}} - \boldsymbol{\Phi}_{\mathrm{R}})\left|\boldsymbol{\Phi}_{\mathrm{R,superbee}} - \boldsymbol{\Phi}_{\mathrm{R}}\right|} \min\left[a\frac{|\boldsymbol{\Phi}_{\mathrm{L}} - \boldsymbol{\Phi}_{\mathrm{R}}|}{2}, \left|\boldsymbol{\Phi}_{\mathrm{R,superbee}} - \boldsymbol{\Phi}_{\mathrm{R}}\right|\right], \tag{27b}$$

where $a = 1 - \min(1,\max(|M_{\mathrm{L}}|,|M_{\mathrm{R}}|))^2$, and its derivative is continuous when the Mach number becomes zero. In supersonic flows, the function a has the value of zero and

$$\boldsymbol{\Phi}_{\mathrm{L},\frac{1}{2}} = \boldsymbol{\Phi}_{\mathrm{L}}, \quad \boldsymbol{\Phi}_{\mathrm{R},\frac{1}{2}} = \boldsymbol{\Phi}_{\mathrm{R}}. \tag{28}$$

Although, the analysis in this section is carried out using TVD limiters, the Proposition looks general in the sense that the present approach is still available when other monotonic interpolation schemes are adopted, such as ENO and multi-dimensional process (MLP) that will be developed in Part II.

2.3. Monotonicity

2.3.1. Modification of the functions w and f

In AUSMPW+, shock discontinuity is recognized using the pressure based weight function by which the advection property is controlled to remove overshoot phenomena. In most cases, it is useful and very effective. However, in weak shock discontinuity, pressure is no longer a good indicator due to small pressure difference. To improve this situation, the Mach number is introduced to determine the final form of w.

The function w is given as follows:

$$w = \max\left[w_1, w_2\right]. \tag{29}$$

In case of steady flow

$$w_1 = \left[\min\left(\sqrt{\frac{\gamma-1}{\gamma+1}}, \max\left(|M_{\mathrm{L}}^*|, |M_{\mathrm{R}}^*|\right)\right)\sqrt{\frac{\gamma+1}{\gamma-1}}\right]^2, \tag{30a}$$

where superscript $*$ indicates sonic property.

In case of unsteady flow

$$w_1 = 1 - \min\left(\frac{p_{\mathrm{L}}}{p_{\mathrm{R}}}, \frac{p_{\mathrm{R}}}{p_{\mathrm{L}}}\right)^3. \tag{30b}$$

When there is shock instability, it is completely avoided by adding the following term, which is optional. Along the ξ direction (see Fig. 4)

$$w_2 = \left[1 - \min\left(1, \frac{\bar{p}_{i+1,j} - \bar{p}_{i,j}}{0.25\left(\bar{p}_{i+1,j+1} + \bar{p}_{i,j+1} - \bar{p}_{i+1,j-1} - \bar{p}_{i,j-1}\right)}\right)\right]^2 \left[1 - \min\left(\frac{\bar{p}_{i,j}}{\bar{p}_{i+1,j}}, \frac{\bar{p}_{i+1,j}}{\bar{p}_{i,j}}\right)\right]^2. \tag{31a}$$

Along the η direction

$$w_2 = \left[1 - \min\left(1, \frac{\bar{p}_{i,j+1} - \bar{p}_{i,j}}{0.25\left(\bar{p}_{i+1,j+1} + \bar{p}_{i+1,j} - \bar{p}_{i-1,j+1} - \bar{p}_{i-1,j}\right)}\right)\right]^2 \left[1 - \min\left(\frac{\bar{p}_{i,j}}{\bar{p}_{i,j+1}}, \frac{\bar{p}_{i,j+1}}{\bar{p}_{i,j}}\right)\right]^2. \tag{31b}$$

In Eq. (29), w_1 detects whether shock exists in the normal direction to a cell-interface or not.

In case of stationary shock wave, it is detected by Mach number relation. As the Mach number in front of shock increases infinitely, the characteristic Mach number M^* employed in w_1 is converged to the finite value, $\sqrt{(\gamma+1)/(\gamma-1)}$ as in Eq. (32). Thus, from the Prandtl relation, shock discontinuity can exist only if the Mach numbers of cells are greater than $\sqrt{(\gamma-1)/(\gamma+1)}$. In this region, w_1 has the value of one. Elsewhere, w_1 is the function of the critical Mach number, and it becomes zero as the Mach number goes to zero to capture the contact discontinuity without numerical dissipation

$$M_1 = \frac{u_1}{c_1} \to \infty, \quad M_1^* = \frac{u_1}{c^*} \to \sqrt{\frac{\gamma+1}{\gamma-1}}, \quad M_2^* = \frac{u_2}{c^*} \to \sqrt{\frac{\gamma-1}{\gamma+1}}. \tag{32}$$

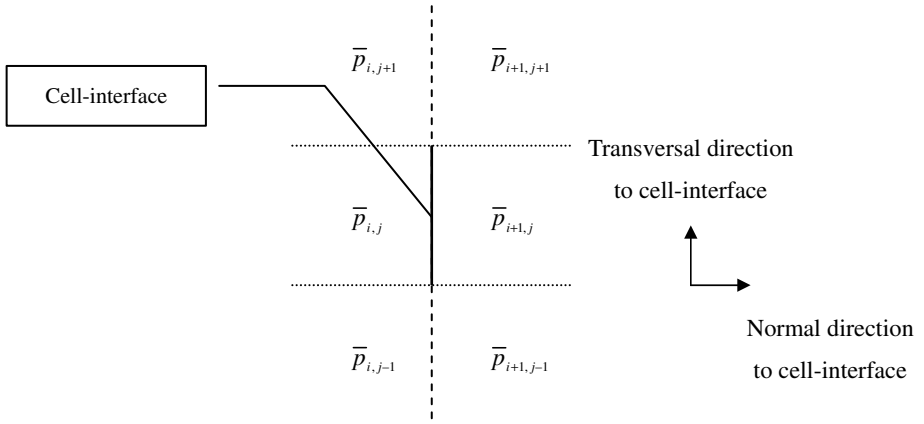

Fig. 4. Pressure distribution around a cell-interface.

Here, $M_{1,2}$ and $M^*_{1,2}$ denotes Mach numbers across shock wave when it is treated as pure mathematical discontinuity in gas dynamics. In case of unsteady shock wave, it is detected by pressure ratio, which is identical to AUSMPW+. The detail is referred to [1]. w_2 is the indicator whether a shock exists in the transversal direction to a cell-interface or not, which is necessary to prevent the shock instability phenomenon such as the carbuncle phenomenon. The first term of Eq. (31) detects the degree of shock wave alignment with respect to a cell-interface. If shock is aligned well, it becomes one because $\bar{p}_{i+1,j} - \bar{p}_{i,j}$ is zero. The second term just checks if or not shock wave exists in the transversal direction to a cell-interface. And, the function f is given by

$$f_{\mathrm{L,R}} = \begin{cases} \left(\frac{p_{\mathrm{L,R}}}{p_s} - 1\right)(1 - w_2), & p_s \neq 0, \\ 0, & \text{elsewhere}, \end{cases} \tag{33}$$

where $p_s = p_{\mathrm{L}} P^+_{\mathrm{L}} + p_{\mathrm{R}} P^-_{\mathrm{R}}$.

2.3.2. Modification of the pressure splitting function

The advection property of AUSM-type schemes may lead to undesirable overshoot problems across shock discontinuity. Fig. 5 shows the typical profiles of numerical shock wave in one-point shock capturing schemes, where the ith cell is intermediate. Fig. 6 shows corresponding converged pressure distribution at the $(i + 1)$th cell according to the intermediate Mach number of cell i, when the left and right physical states across the shock wave are fixed. It is found out that the converged pressure distribution of AUSM+ changes rapidly in case of $M^*_i \approx M^*_1$ or $M^*_i \approx M^*_2$, i.e., when the location of a cell-interface almost coincides with the position of shock discontinuity. In other words, pressure rapidly changes even if the Mach number changes gently. Thus, if a cell-interface is nearly aligned with physical shock wave, there is a danger that convergence becomes deteriorated. Moreover, numerical dissipation across sonic transition position disappears in a shock-aligned grid system, which also makes convergence even worse. For these reasons, it is often observed that convergence is very sensitive to grid system if $M^*_i \approx M^*_1$ or $M^*_i \approx M^*_2$.

Fig. 7 is a good example showing the sensitivity of grid convergence. Depending on the location of sonic transition point with respect to a cell-interface, the behavior of computed solutions is quite different. In the initial stage of computation, numerical shock is propagated from the wall and moves toward steady shock

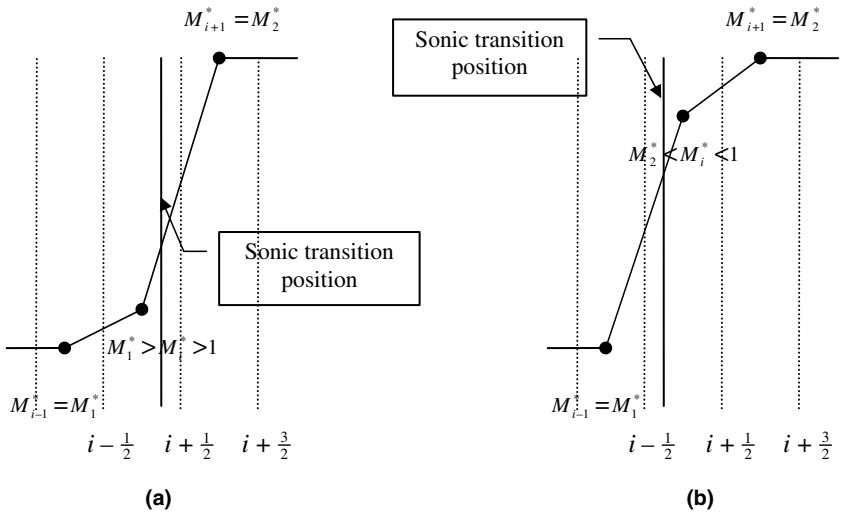

Fig. 5. Numerical shock profile of one point shock capturing scheme.

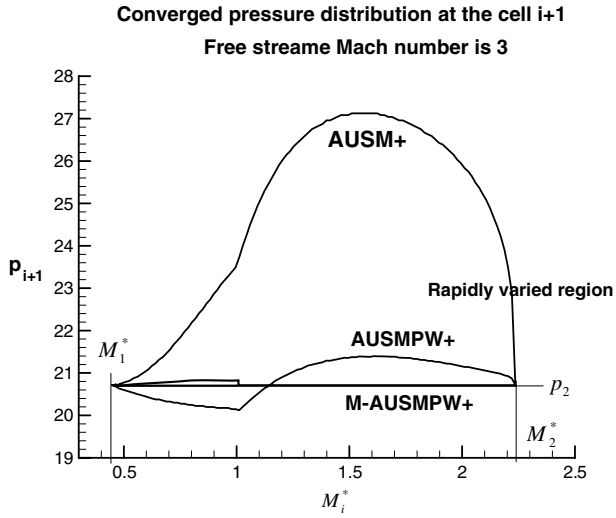

Fig. 6. Comparison of pressure overshoots according to the Mach number at an intermediate cell.

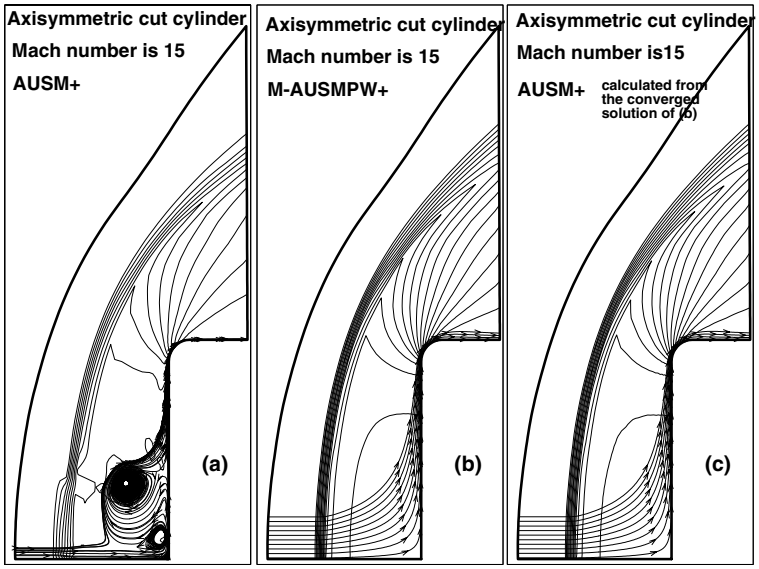

Fig. 7. Pressure contours and streamlines around a cut cylinder.

location. During this evolution, stagnation region is continuously exposed to numerical error generated by numerical shock wave, and contaminated stagnation region changes shock location again. In this situation, if pressure changes rapidly according to the Mach number at the intermediate cell, it is very difficult to obtain a converged solution. At the worst case, a converged solution cannot be obtained at all like Fig. 7(a). In order to prevent this phenomenon completely, the interaction between shock discontinuity and stagnation region due to numerical error should be eliminated. Fig. 7(c) shows the converged result by AUSM+, which is obtained from the converged result of Fig. 7(b) by M-AUSMPW+.

The pressure splitting function is modified to reduce grid dependency and improve convergence characteristics in steady shock discontinuity. Most useful relations in realizing a numerical shock profile are the Rankine–Hugoniot or the Prandtl relation. Roe's FDS exploits the Rankine–Hugoniot relation and AUSM-type schemes use the Prandtl relation. Unlike the Rankine–Hugoniot relation which includes the relation among thermodynamic variables such as density, pressure and temperature, the Prandtl relation does not possess the information. This lack of information does lead to non-monotonic overshoots or slightly diffusive results of a discrete shock profile. In M-AUSMPW+, this defect is cured by the information on pressure jump across a shock, directly derived from the governing equations.

Let us consider a one-dimensional stationary shock wave with $c_s = c^*$. Then, from the Prandtl relation, $M_1^* M_2^* = 1$. It is assumed that shock is captured with only one intermediate cell and sonic transition position is located between ith cell and the cell-interface $i+\frac{1}{2}$, as in Fig. 5(a). Then

$$F_{i+\frac{1}{2}} = F_{i+\frac{3}{2}} = u_2 \boldsymbol{\Psi}_2 + \boldsymbol{P}_2. \tag{34}$$

Here, $u_2\boldsymbol{\Psi}_2 + \boldsymbol{P}_2$ denotes the physical flux after shock wave. Thus:

$$U_i \boldsymbol{\Psi}_i + M^-_{i+1} c_{i+\frac{1}{2}} \boldsymbol{\Psi}_{i+1} + \boldsymbol{P}_i + \boldsymbol{P}_{i+1} P^-_{i+1} = U_{i+1}\boldsymbol{\Psi}_{i+1} + \boldsymbol{P}_{i+1} = U_2 \boldsymbol{\Psi}_2 + \boldsymbol{P}_2, \tag{35a}$$

$$U_i \boldsymbol{\Psi}_i + \boldsymbol{P}_i = M^+_{i+1} c_{i+\frac{1}{2}} \boldsymbol{\Psi}_{i+1} + \boldsymbol{P}_{i+1} P^+_{i+1}. \tag{35b}$$

Continuity equation

$$\rho_i U_i = \rho_{i+1} M^+_{i+1} c_{i+\frac{1}{2}}. \tag{36a}$$

Momentum equation

$$\rho_i U_i U_i + p_i = \rho_{i+1} M^+_{i+1} c_{i+\frac{1}{2}} U_{i+1} + \left(1 - P^-_{i+1}\right) p_{i+1}. \tag{36b}$$

Energy equation

$$\rho_i U_i H_i = \rho_{i+1} M^+_{i+1} c_{i+\frac{1}{2}} H_{i+1}. \tag{36c}$$

Since the total enthalpy should be constant in a steady flow, energy equation is always satisfied only if continuity equation is satisfied. From Eqs. (36a) and (36b), the information on pressure jump across a shock can be obtained as follows:

$$\rho_i U_i U_i + p_i = \rho_i U_i U_{i+1} + \left(1 - P^-_{i+1}\right) p_{i+1}, \tag{37a}$$

$$P^-_{i+1} = 1 - \frac{\rho_i U_i (U_i - U_{i+1}) + p_i}{p_{i+1}}. \tag{37b}$$

Eq. (37) compensates the missing information among thermodynamic variables across shock. In case of Fig. 5(b), pressure splitting function does not need to be modified since shock turns out to be stable and maintains a monotonic profile [13]. Thus, the modified form of pressure splitting function is written as follows:

If $M_i^* > 1$, $M_{i+1}^* < 1$ and $0 < M_i^* M_{i+1}^* < 1$

$$P^-_{i+1} = 1 - \frac{\rho_i U_i (U_i - U_{i+1}) + p_i}{p_{i+1}}. \tag{38a}$$

If $M_i^* > -1$, $M_{i+1}^* < -1$ and $0 < M_i^* M_{i+1}^* < 1$

$$P^+_i = 1 - \frac{\rho_{i+1} U_{i+1} (U_{i+1} - U_i) + p_{i+1}}{p_i}. \tag{38b}$$

Otherwise, it keeps the original form of Eq. (4).

If computation reaches a steady state, Eq. (38) is distributed as in Fig. 8 showing that the positivity of the modified pressure splitting function. In transient process to obtain a steady state solution, however, the positivity of Eq. (38) may not be guaranteed due to numerical error. Thus, the following form is adopted just for stable computation:

If $M_i^* > 1$, $M_{i+1}^* < 1$ and $0 < M_i^* M_{i+1}^* < 1$

$$P_{i+1}^- = \max\left(0, \min\left(0.5, 1 - \frac{\rho_i U_i (U_i - U_{i+1}) + p_i}{p_{i+1}}\right)\right). \tag{39a}$$

If $M_i^* > -1$, $M_{i+1}^* < -1$ and $0 < M_i^* M_{i+1}^* < 1$

$$P_i^+ = \max\left(0, \min\left(0.5, 1 - \frac{\rho_{i+1} U_{i+1} (U_{i+1} - U_i) + p_{i+1}}{p_i}\right)\right). \tag{39b}$$

Figs. 6 and 7(b) clearly show the effect of the modified pressure splitting function.

The modification of the pressure splitting function can be examined in several flow conditions. Let us consider the four different cases at a cell-interface across sonic transition position: compression shock wave, expansion shock wave, continuous compression flow, and continuous expansion flow.

In case of expansion flows, the modification is not turned on. Since the derivative of the original pressure splitting function is continuous, a continuous solution can be obtained. Especially, the present scheme does not admit expansion shock condition by the proper action of numerical dissipation [1].

In case of compression shock, the derivative of the modified pressure splitting function is discontinuous across sonic transition position. The derivative does not have to be continuous in numerical shock region. Numerical shock wave is always captured with some intermediate states. Contrary to flow physics, numerical mass flux at the intermediate cell cannot be conserved. Thus, the property at the intermediate cell can be treated as purely numerical values, i.e., there is no physical meaning. If the pressure splitting function is modified, it just means that the property at the intermediate cell is determined just for the purpose of numerical stability. In this respect, the modification never makes a problem even if its first derivative is

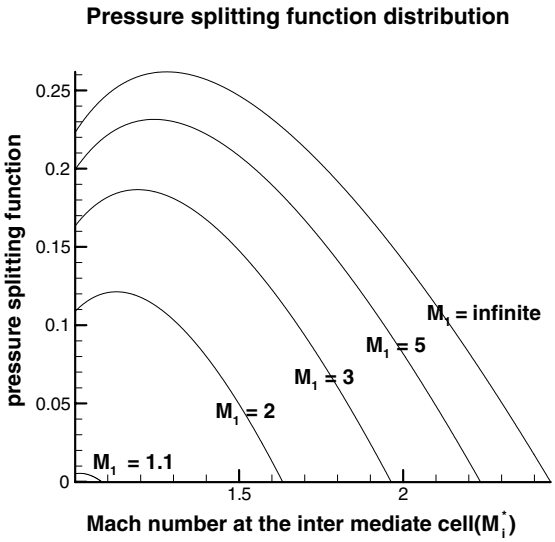

Fig. 8. Plot of pressure splitting function (Eq. (38)) according to the Mach number at an intermediate cell.

not continuous. Lastly, in case of continuous compression wave, the non-smoothness may generate some problem. In actual computations, it does not cause any problem especially when a higher order spatial accuracy is used. Since left and the right values are very close to each other, $p_L \approx p_R$ and $M_{L,R} \approx 1$ and $P_R^- \to 0$ or $M_{L,R} \approx -1$ and $P_L^+ \to 0$. As a consequence, the modification is useful for a steady flow calculation and grid dependency is considerably reduced.

Even though the modification is derived under steady flow assumption, it can be used optionally for unsteady cases. It works successfully in unsteady shock wave without any numerical instability, which is verified with moving shock wave in Section 4.2.

Summarizing the previous analyses, the M-AUSMPW+ can be written as follows:

$$\mathbf{F}_{\frac{1}{2}} = \bar{M}_L^+ c_{\frac{1}{2}} \boldsymbol{\Psi}_{L,\frac{1}{2}} + \bar{M}_R^- c_{\frac{1}{2}} \boldsymbol{\Psi}_{R,\frac{1}{2}} + \left(P_L^+ \boldsymbol{P}_L + P_R^- \boldsymbol{P}_R\right),$$

where $\boldsymbol{P}_{L,R} = (0, n_x p_{L,R}, n_y p_{L,R}, 0)^T$ and $n_{x,y}$ are the components of (x,y) normal vector of a cell-interface.

The convective vector, $\boldsymbol{\Psi}$ are

$$\boldsymbol{\Psi}_{L,R,\frac{1}{2}} = \begin{pmatrix} \rho_{L,R,\frac{1}{2}} \\ \rho_{L,R,\frac{1}{2}} u_{L,R,\frac{1}{2}} \\ \rho_{L,R,\frac{1}{2}} v_{L,R,\frac{1}{2}} \\ \rho_{L,R,\frac{1}{2}} H_{L,R,\frac{1}{2}} \end{pmatrix},$$

where $H_{L,R,\frac{1}{2}} = \frac{\gamma}{\gamma-1} \frac{p_{L,R,\frac{1}{2}}}{\rho_{L,R,\frac{1}{2}}} + 0.5(u^2_{L,R,\frac{1}{2}} + v^2_{L,R,\frac{1}{2}})$. Re-evaluated quantities at a cell-interface are obtained from Eq. (27). $\bar{M}^{\pm}_{L,R}$, $P^{\pm}_{L,R}$ and the speed of sound at a cell-interface are the same as in AUSMPW+ in Section 2.1. In this process, pressure based weighting function (Eqs. (29) and (33)) and the modified pressure splitting function Eq. (39) are employed.

3. Characteristics of M-AUSMPW+

In this section, the numerical properties of M-AUSMPW+ are analyzed from the viewpoint of accuracy, robustness and efficiency.

3.1. Accuracy enhancement in physical discontinuities

3.1.1. Contact or slip discontinuity

Employing the form of first order spatial accuracy, the numerical dissipation of AUSMPW+ and M-AUSMPW+ is written as follows:

$$\mathbf{F}_{\frac{1}{2},\text{AUSMPW+}} = \boldsymbol{\Psi}_{i \text{ or } i+1}\left(M_L^+ + M_R^-\right)c_{\frac{1}{2}} + \boldsymbol{P}_i P_i^+ + \boldsymbol{P}_{i+1} P_{i+1}^- = \boldsymbol{\Psi}_i U_i + \boldsymbol{P}_i P_i^+ + \boldsymbol{P}_{i+1} P_{i+1}^-. \tag{40a}$$

$$\mathbf{F}_{\frac{1}{2},\text{M-AUSMPW+}} = \boldsymbol{\Psi}_{L,\frac{1}{2}}\left(M_L^+ + M_R^-\right)c_{\frac{1}{2}} + \boldsymbol{P}_i P_i^+ + \boldsymbol{P}_{i+1} P_{i+1}^- = \boldsymbol{\Psi}_{L,\frac{1}{2}} U_i + \boldsymbol{P}_i P_i^+ + \boldsymbol{P}_{i+1} P_{i+1}^-. \tag{40b}$$

Across contact or slip discontinuity, velocity and pressure are the same

$$U_i = U_{i+1}, \quad p_i = p_{i+1}.$$

Thus, only the convective flux is analyzed here. The diffusive flux part of the convective flux showing the magnitude of numerical dissipation explicitly is

$$\mathbf{F}_{\frac{1}{2},\text{convective}} = 0.5\left(\bar{\boldsymbol{\Phi}}_i U_i + \bar{\boldsymbol{\Phi}}_{i+1} U_{i+1}\right) - \boldsymbol{D}. \tag{41}$$

Assuming U is positive, the numerical viscosity of each scheme can be written as follows:

$$\frac{\boldsymbol{D}_{\text{AUSMPW+}}}{(\bar{\boldsymbol{\Phi}}_{i+1}-\bar{\boldsymbol{\Phi}}_i)}=\frac{0.5\left(\bar{\boldsymbol{\Phi}}_i U_i+\bar{\boldsymbol{\Phi}}_{i+1}U_{i+1}-2\bar{\boldsymbol{\Phi}}_i\left(M_i^+ + M_{i+1}^-\right)c_{\frac{1}{2}}\right)}{(\bar{\boldsymbol{\Phi}}_{i+1}-\bar{\boldsymbol{\Phi}}_i)}=0.5U_i. \tag{42a}$$

$$\frac{\boldsymbol{D}_{\text{M-AUSMPW+}}}{(\bar{\boldsymbol{\Phi}}_{i+1}-\bar{\boldsymbol{\Phi}}_i)}=\frac{0.5\left(\bar{\boldsymbol{\Phi}}_i U_i+\bar{\boldsymbol{\Phi}}_{i+1}U_{i+1}-2\boldsymbol{\Phi}_{\text{L},\frac{1}{2}}\left(M_i^+ + M_{i+1}^-\right)c_{\frac{1}{2}}\right)}{(\bar{\boldsymbol{\Phi}}_{i+1}-\bar{\boldsymbol{\Phi}}_i)}=0.5U_i\left[1-2\frac{\left(\boldsymbol{\Phi}_{\text{L},\frac{1}{2}}-\bar{\boldsymbol{\Phi}}_i\right)}{(\bar{\boldsymbol{\Phi}}_{i+1}-\bar{\boldsymbol{\Phi}}_i)}\right], \tag{42b}$$

where

$$\boldsymbol{\Phi}_{\text{L},\frac{1}{2}}=\bar{\boldsymbol{\Phi}}_i+\frac{\max\left[0,(\bar{\boldsymbol{\Phi}}_{i+1}-\bar{\boldsymbol{\Phi}}_i)(\boldsymbol{\Phi}_{\text{L,superbee}}-\bar{\boldsymbol{\Phi}}_i)\right]}{(\bar{\boldsymbol{\Phi}}_{i+1}-\bar{\boldsymbol{\Phi}}_i)\left|\boldsymbol{\Phi}_{\text{L,superbee}}-\bar{\boldsymbol{\Phi}}_i\right|}\min\left[a\frac{\left|\bar{\boldsymbol{\Phi}}_{i+1}-\bar{\boldsymbol{\Phi}}_i\right|}{2},\left|\boldsymbol{\Phi}_{\text{L,superbee}}-\bar{\boldsymbol{\Phi}}_i\right|\right].$$

Eq. (42) clearly shows the difference in spatial accuracy between AUSMPW+ and M-AUSMPW+. Employing a higher order spatial accuracy with TVD limiter:

$$\frac{\boldsymbol{D}_{\text{AUSMPW+}}}{(\bar{\boldsymbol{\Phi}}_{i+1}-\bar{\boldsymbol{\Phi}}_i)}=\frac{0.5\left(\bar{\boldsymbol{\Phi}}_i U_i+\bar{\boldsymbol{\Phi}}_{i+1}U_{i+1}-2\boldsymbol{\Phi}_{\text{L}}\left(M_{\text{L}}^+ + M_{\text{R}}^-\right)c_{\frac{1}{2}}\right)}{(\bar{\boldsymbol{\Phi}}_{i+1}-\bar{\boldsymbol{\Phi}}_i)}=0.5U_i\left[1-2\frac{(\boldsymbol{\Phi}_{\text{L}}-\bar{\boldsymbol{\Phi}}_i)}{(\bar{\boldsymbol{\Phi}}_{i+1}-\bar{\boldsymbol{\Phi}}_i)}\right], \tag{43a}$$

$$\frac{\boldsymbol{D}_{\text{M-AUSMPW+}}}{(\bar{\boldsymbol{\Phi}}_{i+1}-\bar{\boldsymbol{\Phi}}_i)}=\frac{0.5\left(\bar{\boldsymbol{\Phi}}_i U_i+\bar{\boldsymbol{\Phi}}_{i+1}U_{i+1}-2\boldsymbol{\Phi}_{\text{L},\frac{1}{2}}\left(M_{\text{L}}^+ + M_{\text{R}}^-\right)c_{\frac{1}{2}}\right)}{(\bar{\boldsymbol{\Phi}}_{i+1}-\bar{\boldsymbol{\Phi}}_i)}=0.5U_i\left[1-2\frac{\left(\boldsymbol{\Phi}_{\text{L},\frac{1}{2}}-\bar{\boldsymbol{\Phi}}_i\right)}{(\bar{\boldsymbol{\Phi}}_{i+1}-\bar{\boldsymbol{\Phi}}_i)}\right], \tag{43b}$$

where

$$\boldsymbol{\Phi}_{\text{L},\frac{1}{2}}=\boldsymbol{\Phi}_{\text{L}}+\frac{\max\left[0,(\boldsymbol{\Phi}_{\text{R}}-\boldsymbol{\Phi}_{\text{L}})(\boldsymbol{\Phi}_{\text{L,superbee}}-\boldsymbol{\Phi}_{\text{L}})\right]}{(\boldsymbol{\Phi}_{\text{R}}-\boldsymbol{\Phi}_{\text{L}})\left|\boldsymbol{\Phi}_{\text{L,superbee}}-\boldsymbol{\Phi}_{\text{L}}\right|}\min\left[a\frac{\left|\boldsymbol{\Phi}_{\text{R}}-\boldsymbol{\Phi}_{\text{L}}\right|}{2},\left|\boldsymbol{\Phi}_{\text{L,superbee}}-\boldsymbol{\Phi}_{\text{L}}\right|\right].$$

In M-AUSMPW+, the sign of $\boldsymbol{\Phi}_{\text{L},\frac{1}{2}}-\bar{\boldsymbol{\Phi}}_i$ is always the same as that of $\bar{\boldsymbol{\Phi}}_{i+1}-\bar{\boldsymbol{\Phi}}_i$ and the condition of $\frac{\boldsymbol{\Phi}_{\text{L}}-\bar{\boldsymbol{\Phi}}_i}{\bar{\boldsymbol{\Phi}}_{i+1}-\bar{\boldsymbol{\Phi}}_i}\leqslant\frac{\boldsymbol{\Phi}_{\text{L},\frac{1}{2}}-\bar{\boldsymbol{\Phi}}_i}{\bar{\boldsymbol{\Phi}}_{i+1}-\bar{\boldsymbol{\Phi}}_i}$ is always satisfied throughout a numerical discontinuity (see Eq. (27)). Thus, the numerical viscosity of M-AUSMPW+ is always less than that of AUSMPW+. In addition, since $\boldsymbol{\Phi}_{\text{L},\frac{1}{2}}$ satisfies the monotonic constraint of Eq. (23), M-AUSMPW+ maintains monotonicity as well as accuracy improvement.

3.1.2. Oblique contact discontinuity

In Section 2, it was shown that the convective quantity of M-AUSMPW+ yields a closer approximation to the physical value. In this section, another important merit of M-AUSMPW+ is revealed. The basic difference between Eqs. (5) and (6) is examined by analyzing numerical dissipation in multi-dimensional flows. Although the basic idea of M-AUSMPW+ is developed without directly considering multi-dimensional flows, the resulting flux form turns out to be very much effective in the computations of multi-dimensional flows. Fig. 9 shows the schematic of an oblique contact discontinuity which is not aligned with a grid line or a cell-interface. In this case, unnecessary numerical dissipation is generated and the discontinuity is smeared. For this reason, multi-dimensional computations commonly require denser grid systems or a highly accurate numerical scheme.

Let us consider contact discontinuity with constant velocity. In Fig. 10(a), discontinuity is well aligned with grid lines and in Fig. 10(b), the situation is opposite. The initial conditions at cells 1 and 3 are known, but in cell 2, where discontinuity is passing through, they should be determined physically. Since Figs. 10(a) and (b) should represent the same flow physics, the values of cell 2 is reasonable if they satisfy conservation requirements. Then, from mass conservation:

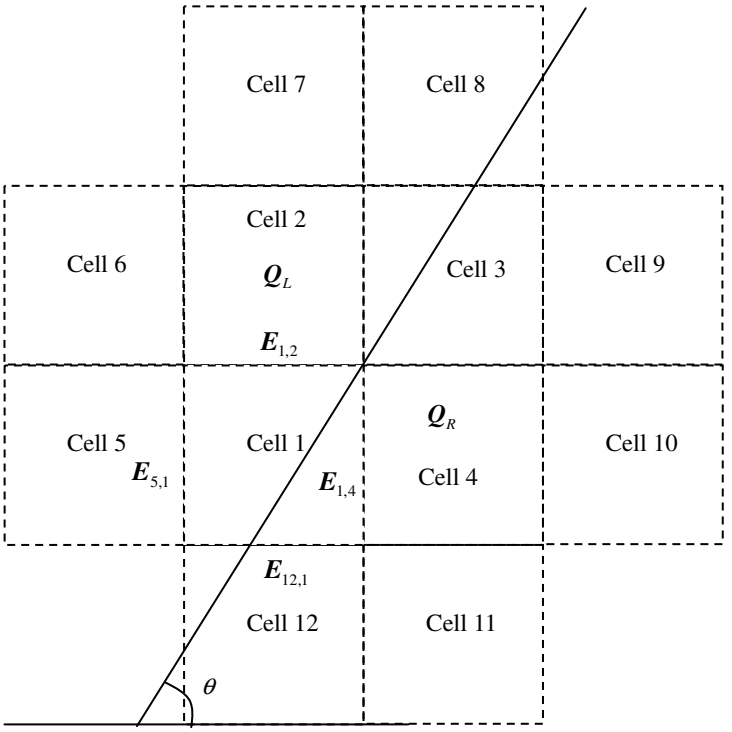

Fig. 9. Schematics of the oblique discontinuity inclined to a cell-interface.

$$(A_1 + A_{2,1})\rho_1 + (A_{2,2} + A_3)\rho_3|_{(a)} = A_1\rho_1 + (A_{2,1} + A_{2,2})\rho_2 + A_3\rho_3|_{(b)}, \tag{44a}$$

$$\rho_2 = \frac{A_{2,1}\rho_1 + A_{2,2}\rho_3}{A_{2,1} + A_{2,2}}. \tag{44b}$$

Through momentum and energy conservation, $\rho \boldsymbol{V}$ and ρe at the cell 2 are given as follows:

$$(A_1 + A_{2,1})\rho_1 \boldsymbol{V}_1 + (A_{2,2} + A_3)\rho_3 \boldsymbol{V}_3|_{(a)} = A_1\rho_1 \boldsymbol{V}_1 + (A_{2,1} + A_{2,2})\rho_2 \boldsymbol{V}_2 + A_3\rho_3 \boldsymbol{V}_3|_{(b)}, \tag{45a}$$

$$\rho_2 \boldsymbol{V}_2 = \frac{A_{2,1}\rho_1 \boldsymbol{V}_1 + A_{2,2}\rho_3 \boldsymbol{V}_3}{A_{2,1} + A_{2,2}}. \tag{45b}$$

All of the internal energies are the same because pressure is constant across contact or slip discontinuity

$$\rho_1 e_1 = \rho_2 e_2 = \rho_3 e_3. \tag{46a}$$

Thus, the total enthalpy in cell 2 is given by

$$\rho_2 H_2 = \rho_2 e_2 + p_2 + 0.5\rho_2 \boldsymbol{V} \cdot \boldsymbol{V} = \rho_2 e_2 + p_2 + 0.5\frac{A_{2,1}\rho_1 + A_{2,2}\rho_3}{A_{2,1} + A_{2,2}} \boldsymbol{V} \cdot \boldsymbol{V} = \frac{A_{2,1}\rho_1 H_1 + A_{2,2}\rho_3 H_3}{A_{2,1} + A_{2,2}}. \tag{46b}$$

From Eqs. (44)–(46), it is reasonable that the initial condition of cell 2 should be specified by the area ratio divided by a contact discontinuity.

Now, let us assume that discontinuity is inclined as in Fig. 9. Then, the discretized governing equation can be written

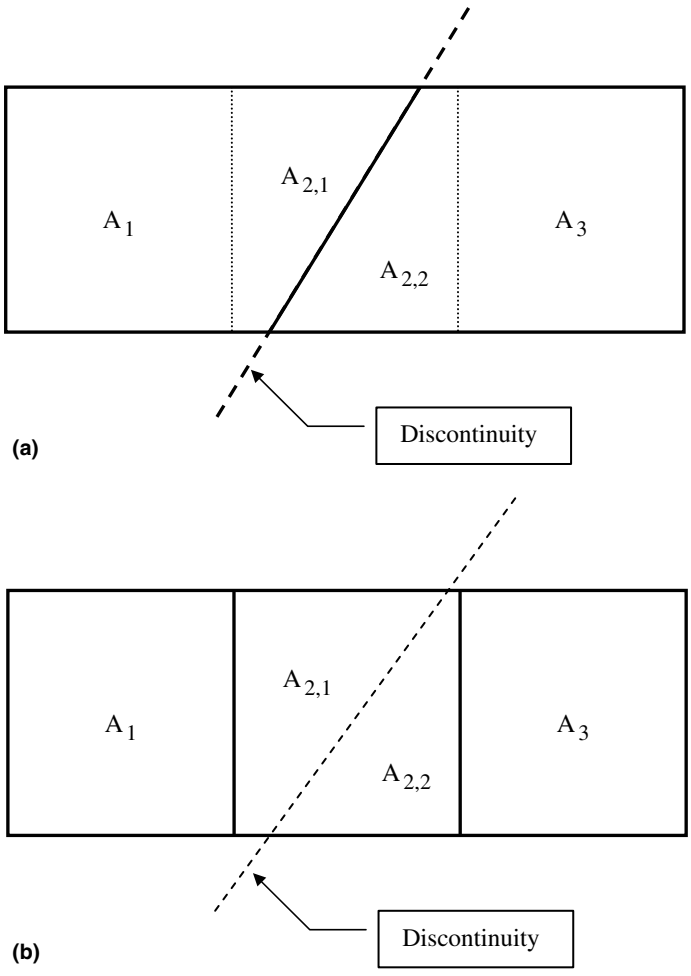

Fig. 10. (a) Cell-interface aligned with a discontinuity. (b) Cell-interface not aligned with a discontinuity.

$$\boldsymbol{Q}^{n+1} = \boldsymbol{Q}^{n} - J\Delta t \oint \boldsymbol{E} \cdot \mathrm{d}s = \boldsymbol{Q}^{n} - J\Delta t \sum \boldsymbol{E} \cdot \Delta s, \tag{47}$$

where $\boldsymbol{Q} = (\rho, \rho u, \rho v, \rho e_t)^{\mathrm{T}}$, $J = 1/V$ and V is a cell area and Δs is the length of a cell-interface. The cells 2, 5, 6 and 7 located on the left side of the discontinuity have the value of $\boldsymbol{\Psi}_{\mathrm{L}}$, and the cells 4, 9, 10 and 11 on the right side of the discontinuity have $\boldsymbol{\Psi}_{\mathrm{R}}$. Properties at the intermediate region are determined by the area ratio divided by the discontinuity as in Fig. 11. Then:

$$\boldsymbol{\Psi}_1 = \left(1 - \frac{0.5}{\tan\theta}\right)\boldsymbol{\Psi}_{\mathrm{L}} + \frac{0.5}{\tan\theta}\boldsymbol{\Psi}_{\mathrm{R}}, \tag{48a}$$

$$\boldsymbol{\Psi}_3 = \left(1 - \frac{0.5}{\tan\theta}\right)\boldsymbol{\Psi}_{\mathrm{R}} + \frac{0.5}{\tan\theta}\boldsymbol{\Psi}_{\mathrm{L}}, \tag{48b}$$

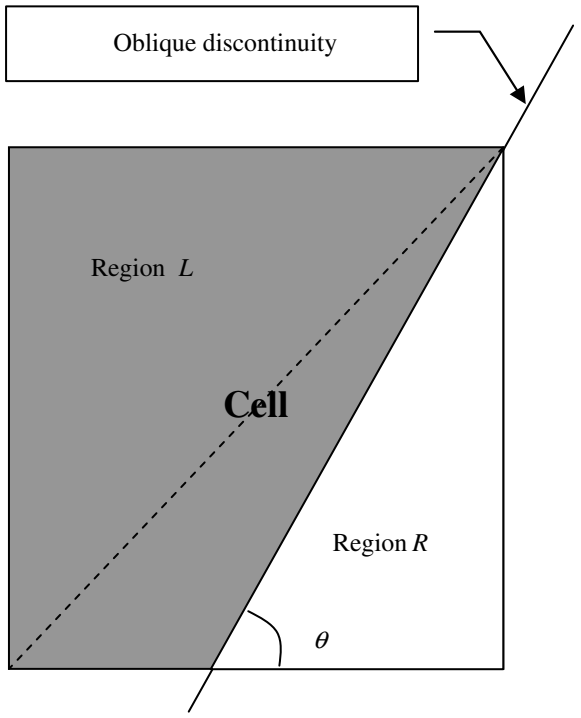

Fig. 11. Cell divided by the oblique discontinuity.

$$\boldsymbol{\Psi}_8 = \begin{cases} 0.5\left(1-\frac{1}{\tan\theta}\right)^2 \tan\theta \boldsymbol{\Psi}_{\mathrm{R}} + \left\{1 - 0.5\left(1-\frac{1}{\tan\theta}\right)^2 \tan\theta\right\}\boldsymbol{\Psi}_{\mathrm{L}}, & 1 \leqslant \tan\theta < 2, \\ \left(1-\frac{3}{2\tan\theta}\right)\boldsymbol{\Psi}_{\mathrm{R}} + \frac{3}{2\tan\theta}\boldsymbol{\Psi}_{\mathrm{L}}, & 2 \leqslant \tan\theta < \infty, \end{cases} \tag{48c}$$

$$\boldsymbol{\Psi}_{12} = \begin{cases} 0.5\left(1-\frac{1}{\tan\theta}\right)^2 \tan\theta \boldsymbol{\Psi}_{\mathrm{L}} + \left\{1 - 0.5\left(1-\frac{1}{\tan\theta}\right)^2 \tan\theta\right\}\boldsymbol{\Psi}_{\mathrm{R}}, & 1 \leqslant \tan\theta < 2, \\ \left(1-\frac{3}{2\tan\theta}\right)\boldsymbol{\Psi}_{\mathrm{L}} + \frac{3}{2\tan\theta}\boldsymbol{\Psi}_{\mathrm{R}}, & 2 \leqslant \tan\theta < \infty, \end{cases} \tag{48d}$$

where $\boldsymbol{\Psi} = (\rho, \rho u, \rho v, \rho H)^{\mathrm{T}}$, H is the total enthalpy and θ is the angle between a discontinuity and a cell-interface. Since $0° < \theta < 45°$ and $45° < \theta < 90°$ are symmetric with each other, only the case of $45° < \theta < 90°$ is considered.

For the following flux form:

$$\mathbf{F}_{\frac{1}{2}} = m_{\frac{1}{2}} c_{\frac{1}{2}} \boldsymbol{\Psi} \tag{49}$$

with $m_{\frac{1}{2}} = M_{\mathrm{L}}^{+} + M_{\mathrm{R}}^{-} > 0$, net flux differences generated in cells 1–4 are given as follows. For convenience, all of the cell-interfaces have unit length.

Case 1: $\boldsymbol{\Psi} = \boldsymbol{\Psi}_{\mathrm{L}}$ (AUSM+ or AUSMPW+)

(i) Cell 1:

$$\begin{aligned} \boldsymbol{Q}_1^{n+1} &= \boldsymbol{Q}_1^{n} - J\Delta t(\boldsymbol{E}_{1,4} + \boldsymbol{E}_{1,2} - \boldsymbol{E}_{5,1} - \boldsymbol{E}_{12,1}) \\ &= \boldsymbol{Q}_1^{n} - J\Delta t(|\boldsymbol{V}|\cos\theta\boldsymbol{\Psi}_1 + |\boldsymbol{V}|\sin\theta\boldsymbol{\Psi}_1 - |\boldsymbol{V}|\cos\theta\boldsymbol{\Psi}_{\mathrm{L}} - |\boldsymbol{V}|\sin\theta\boldsymbol{\Psi}_{12}), \\ &= \boldsymbol{Q}_1^{n} - J\Delta t|\boldsymbol{V}|\{\cos\theta(\boldsymbol{\Psi}_1 - \boldsymbol{\Psi}_{\mathrm{L}}) + \sin\theta(\boldsymbol{\Psi}_1 - \boldsymbol{\Psi}_{12})\}, \end{aligned} \tag{50a}$$

where $\boldsymbol{E}_{1,4}$ means the cell-interface flux whose neighboring cells are 1 and 4 as in Fig. 9.

(ii) Cell 2:

$$\begin{aligned}\boldsymbol{Q}_2^{n+1} &= \boldsymbol{Q}_2^n - J\Delta t(\boldsymbol{E}_{2,3} + \boldsymbol{E}_{2,7} - \boldsymbol{E}_{6,2} - \boldsymbol{E}_{1,2}) \\ &= \boldsymbol{Q}_2^n - J\Delta t(|\boldsymbol{V}|\cos\theta\boldsymbol{\Psi}_{\mathrm{L}} + |\boldsymbol{V}|\sin\theta\boldsymbol{\Psi}_{\mathrm{L}} - |\boldsymbol{V}|\cos\theta\boldsymbol{\Psi}_{\mathrm{L}} - |\boldsymbol{V}|\sin\theta\boldsymbol{\Psi}_1) \\ &= \boldsymbol{Q}_2^n - J\Delta t|\boldsymbol{V}|\sin\theta(\boldsymbol{\Psi}_{\mathrm{L}} - \boldsymbol{\Psi}_1). \end{aligned} \tag{50b}$$

(iii) Cell 3:

$$\begin{aligned}\boldsymbol{Q}_3^{n+1} &= \boldsymbol{Q}_3^n - J\Delta t(\boldsymbol{E}_{3,9} + \boldsymbol{E}_{3,8} - \boldsymbol{E}_{2,3} - \boldsymbol{E}_{4,3}) \\ &= \boldsymbol{Q}_3^n - J\Delta t(|\boldsymbol{V}|\cos\theta\boldsymbol{\Psi}_3 + |\boldsymbol{V}|\sin\theta\boldsymbol{\Psi}_3 - |\boldsymbol{V}|\cos\theta\boldsymbol{\Psi}_{\mathrm{L}} - |\boldsymbol{V}|\sin\theta\boldsymbol{\Psi}_{\mathrm{R}}) \\ &= \boldsymbol{Q}_3^n - J\Delta t|\boldsymbol{V}|\{\cos\theta(\boldsymbol{\Psi}_3 - \boldsymbol{\Psi}_{\mathrm{L}}) + \sin\theta(\boldsymbol{\Psi}_3 - \boldsymbol{\Psi}_{\mathrm{R}})\}. \end{aligned} \tag{50c}$$

(iv) Cell 4:

$$\begin{aligned}\boldsymbol{Q}_4^{n+1} &= \boldsymbol{Q}_4^n - J\Delta t(\boldsymbol{E}_{4,10} + \boldsymbol{E}_{4,3} - \boldsymbol{E}_{1,4} - \boldsymbol{E}_{11,4}) \\ &= \boldsymbol{Q}_4^n - J\Delta t(|\boldsymbol{V}|\cos\theta\boldsymbol{\Psi}_{\mathrm{R}} + |\boldsymbol{V}|\sin\theta\boldsymbol{\Psi}_{\mathrm{R}} - |\boldsymbol{V}|\cos\theta\boldsymbol{\Psi}_1 - |\boldsymbol{V}|\sin\theta\boldsymbol{\Psi}_{\mathrm{R}}) \\ &= \boldsymbol{Q}_4^n - J\Delta t|\boldsymbol{V}|\cos\theta(\boldsymbol{\Psi}_{\mathrm{R}} - \boldsymbol{\Psi}_1). \end{aligned} \tag{50d}$$

If grid system is exactly aligned with discontinuity as in Fig. 10(a), the initial distribution would be the final solution and discontinuity is exactly maintained. Also, the flux differences of Eq. (50), $J\Delta t\sum \boldsymbol{E}\cdot\Delta s$, become zero. On the other hand, if grid system is not aligned as in Fig. 10(b), the initial condition given from Eq. (44) to Eq. (46) is no longer the final solution. The ideal case would be that $J\Delta t\sum \boldsymbol{E}\cdot\Delta s$ becomes zero and initial condition is accepted as the final solution. It means that, as $J\Delta t\sum \boldsymbol{E}\cdot\Delta s$ becomes smaller, the solution becomes more accurate. In this respect, the sum of net fluxes is a good indicator to show the accuracy of contact discontinuity in non-aligned grid system. The flux difference in each cell, $\boldsymbol{D}$, can be summarized as follows.

(i) Cell 1:

when $1 \leqslant \tan\theta < 2$

$$\begin{aligned}\frac{\boldsymbol{D}_1}{J\Delta t|\boldsymbol{V}|(\boldsymbol{\Psi}_{\mathrm{R}} - \boldsymbol{\Psi}_{\mathrm{L}})} &= -\cos\theta\frac{(\boldsymbol{\Psi}_1 - \boldsymbol{\Psi}_{\mathrm{L}})}{(\boldsymbol{\Psi}_{\mathrm{R}} - \boldsymbol{\Psi}_{\mathrm{L}})} - \sin\theta\frac{(\boldsymbol{\Psi}_1 - \boldsymbol{\Psi}_{12})}{(\boldsymbol{\Psi}_{\mathrm{R}} - \boldsymbol{\Psi}_{\mathrm{L}})} \\ &= \sin\theta - \frac{0.5\cos\theta}{\tan\theta} - 0.5\cos\theta - 0.5\left(1 - \frac{1}{\tan\theta}\right)^2\sin\theta\tan\theta, \end{aligned} \tag{51a}$$

when $2 \leqslant \tan\theta < \infty$

$$\frac{\boldsymbol{D}_1}{J\Delta t|\boldsymbol{V}|(\boldsymbol{\Psi}_{\mathrm{R}} - \boldsymbol{\Psi}_{\mathrm{L}})} = -\cos\theta\frac{(\boldsymbol{\Psi}_1 - \boldsymbol{\Psi}_{\mathrm{L}})}{(\boldsymbol{\Psi}_{\mathrm{R}} - \boldsymbol{\Psi}_{\mathrm{L}})} - \sin\theta\frac{(\boldsymbol{\Psi}_1 - \boldsymbol{\Psi}_{12})}{(\boldsymbol{\Psi}_{\mathrm{R}} - \boldsymbol{\Psi}_{\mathrm{L}})} = \cos\theta\left(1 - \frac{0.5}{\tan\theta}\right). \tag{51b}$$

(ii) Cell 2:

$$\frac{\boldsymbol{D}_2}{J\Delta t|\boldsymbol{V}|(\boldsymbol{\Psi}_{\mathrm{R}} - \boldsymbol{\Psi}_{\mathrm{L}})} = -\sin\theta\frac{(\boldsymbol{\Psi}_{\mathrm{L}} - \boldsymbol{\Psi}_1)}{(\boldsymbol{\Psi}_{\mathrm{R}} - \boldsymbol{\Psi}_{\mathrm{L}})} = 0.5\cos\theta. \tag{51c}$$

(iii) Cell 3:

$$\frac{\boldsymbol{D}_3}{J\Delta t|\boldsymbol{V}|(\boldsymbol{\Psi}_{\mathrm{R}} - \boldsymbol{\Psi}_{\mathrm{L}})} = -\cos\theta\frac{(\boldsymbol{\Psi}_3 - \boldsymbol{\Psi}_{\mathrm{L}})}{(\boldsymbol{\Psi}_{\mathrm{R}} - \boldsymbol{\Psi}_{\mathrm{L}})} - \sin\theta\frac{(\boldsymbol{\Psi}_3 - \boldsymbol{\Psi}_{\mathrm{R}})}{(\boldsymbol{\Psi}_{\mathrm{R}} - \boldsymbol{\Psi}_{\mathrm{L}})} = -\left(\cos\theta\left(1 - \frac{0.5}{\tan\theta}\right) - 0.5\cos\theta\right). \tag{51d}$$

(iv) Cell 4:

$$\frac{\boldsymbol{D}_4}{J\Delta t|\boldsymbol{V}|(\boldsymbol{\Psi}_R-\boldsymbol{\Psi}_L)}=-\cos\theta\frac{(\boldsymbol{\Psi}_R-\boldsymbol{\Psi}_1)}{(\boldsymbol{\Psi}_R-\boldsymbol{\Psi}_L)}=-\cos\theta\left(1-\frac{0.5}{\tan\theta}\right). \tag{51e}$$

Figs. 12(a) and (b) show the distribution of $\boldsymbol{D}$ of AUSMPW+ and Roe's FDS, respectively. The result of Roe's FDS was obtained numerically. AUSMPW+ and Roe's FDS give nearly the same results, implying that AUSMPW+ and Roe's FDS will show almost the same accuracy in capturing an oblique contact discontinuity.

It can be seen from Eqs. (51a)–(51e) that $\boldsymbol{D}$ reduces and finally becomes zero as $\theta\to 90°$, i.e., a grid line is aligned with the discontinuity. In order for $\boldsymbol{D}$ to be zero regardless of θ, the condition of $\boldsymbol{\Psi}_1=\boldsymbol{\Psi}_{12}=\boldsymbol{\Psi}_L$, $\boldsymbol{\Psi}_1=\boldsymbol{\Psi}_L$, $\boldsymbol{\Psi}_3=\boldsymbol{\Psi}_L=\boldsymbol{\Psi}_R$ and $\boldsymbol{\Psi}_1=\boldsymbol{\Psi}_R$ should be satisfied, which is impossible because $\boldsymbol{\Psi}_1$ and $\boldsymbol{\Psi}_3$ cannot be equal to $\boldsymbol{\Psi}_L$ and $\boldsymbol{\Psi}_R$ simultaneously. Thus, the initial condition cannot be the final solution under this formulation because of numerical dissipation. Also, the overall flux difference becomes larger as $\theta\to 45°$, i.e., as multi-dimensional effect increases. Thus, a scheme is more favorable in multi-dimensional problems if $\boldsymbol{D}$ becomes smaller as $\theta\to 45°$. Next, let us consider the averaged value of $\boldsymbol{\Psi}_L$ and $\boldsymbol{\Psi}_R$.

Case 2: $\boldsymbol{\Psi}_{\frac{1}{2}}=\frac{1}{2}(\boldsymbol{\Psi}_L+\boldsymbol{\Psi}_R)$.

(i) Cell 1:

$$\begin{aligned}\boldsymbol{Q}_1^{n+1}&=\boldsymbol{Q}_1^n-J\Delta t(\boldsymbol{E}_{1,4}+\boldsymbol{E}_{1,2}-\boldsymbol{E}_{5,1}-\boldsymbol{E}_{12,1})\\&=\boldsymbol{Q}_1^n-0.5J\Delta t|\boldsymbol{V}|(\cos\theta(\boldsymbol{\Psi}_1+\boldsymbol{\Psi}_R)+\sin\theta(\boldsymbol{\Psi}_1+\boldsymbol{\Psi}_L)-\cos\theta(\boldsymbol{\Psi}_L+\boldsymbol{\Psi}_1)-\sin\theta(\boldsymbol{\Psi}_{12}+\boldsymbol{\Psi}_1))\\&=\boldsymbol{Q}_1^n-0.5J\Delta t|\boldsymbol{V}|\{\cos\theta(\boldsymbol{\Psi}_R-\boldsymbol{\Psi}_L)+\sin\theta(\boldsymbol{\Psi}_L-\boldsymbol{\Psi}_{12})\}.\end{aligned} \tag{52a}$$

(ii) Cell 2:

$$\begin{aligned}\boldsymbol{Q}_2^{n+1}&=\boldsymbol{Q}_2^n-J\Delta t(\boldsymbol{E}_{2,3}+\boldsymbol{E}_{2,7}-\boldsymbol{E}_{6,2}-\boldsymbol{E}_{1,2})\\&=\boldsymbol{Q}_2^n-0.5J\Delta t|\boldsymbol{V}|(\cos\theta(\boldsymbol{\Psi}_L+\boldsymbol{\Psi}_3)+\sin\theta(\boldsymbol{\Psi}_L+\boldsymbol{\Psi}_L)-\cos\theta(\boldsymbol{\Psi}_L+\boldsymbol{\Psi}_L)-\sin\theta(\boldsymbol{\Psi}_1+\boldsymbol{\Psi}_L))\\&=\boldsymbol{Q}_2^n-0.5J\Delta t|\boldsymbol{V}|\{\cos\theta(\boldsymbol{\Psi}_3-\boldsymbol{\Psi}_L)+\sin\theta(\boldsymbol{\Psi}_L-\boldsymbol{\Psi}_1)\}.\end{aligned} \tag{52b}$$

(iii) Cell 3:

$$\begin{aligned}\boldsymbol{Q}_3^{n+1}&=\boldsymbol{Q}_3^n-J\Delta t(\boldsymbol{E}_{3,9}+\boldsymbol{E}_{3,8}-\boldsymbol{E}_{2,3}-\boldsymbol{E}_{4,3})\\&=\boldsymbol{Q}_3^n-0.5J\Delta t|\boldsymbol{V}|(\cos\theta(\boldsymbol{\Psi}_3+\boldsymbol{\Psi}_R)+\sin\theta(\boldsymbol{\Psi}_3+\boldsymbol{\Psi}_8)-\cos\theta(\boldsymbol{\Psi}_L+\boldsymbol{\Psi}_3)-\sin\theta(\boldsymbol{\Psi}_R+\boldsymbol{\Psi}_3))\\&=\boldsymbol{Q}_3^n-0.5J\Delta t|\boldsymbol{V}|\{\cos\theta(\boldsymbol{\Psi}_R-\boldsymbol{\Psi}_L)+\sin\theta(\boldsymbol{\Psi}_8-\boldsymbol{\Psi}_R)\}.\end{aligned} \tag{52c}$$

(iv) Cell 4:

$$\begin{aligned}\boldsymbol{Q}_4^{n+1}&=\boldsymbol{Q}_4^n-J\Delta t(\boldsymbol{E}_{4,10}+\boldsymbol{E}_{4,3}-\boldsymbol{E}_{1,4}-\boldsymbol{E}_{11,4})\\&=\boldsymbol{Q}_4^n-0.5J\Delta t|\boldsymbol{V}|(\cos\theta(\boldsymbol{\Psi}_R+\boldsymbol{\Psi}_R)+\sin\theta(\boldsymbol{\Psi}_R+\boldsymbol{\Psi}_3)-\cos\theta(\boldsymbol{\Psi}_1+\boldsymbol{\Psi}_R)-\sin\theta(\boldsymbol{\Psi}_R+\boldsymbol{\Psi}_R))\\&=\boldsymbol{Q}_4^n-0.5J\Delta t|\boldsymbol{V}|\{\cos\theta(\boldsymbol{\Psi}_R-\boldsymbol{\Psi}_1)+\sin\theta(\boldsymbol{\Psi}_3-\boldsymbol{\Psi}_R)\}.\end{aligned} \tag{52d}$$

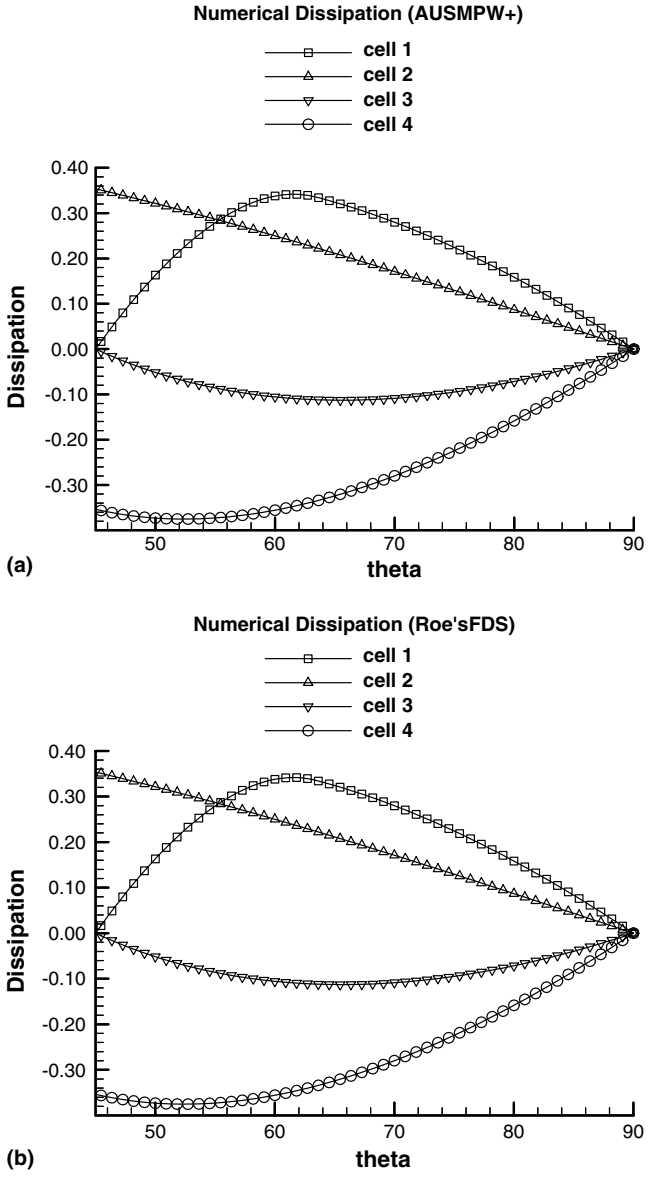

Fig. 12. (a) Numerical dissipation in each cell (AUSM+ or AUSMPW+). (b) Numerical dissipation in each cell (Roe's FDS).

By the same way, the flux difference is summarized as follows:

(i) Cell 1:
when $1 \leqslant \tan\theta < 2$

$$\frac{\boldsymbol{D}_1}{J\Delta t|\boldsymbol{V}|(\boldsymbol{\Psi}_R - \boldsymbol{\Psi}_L)} = 0.5\left(\sin\theta - \cos\theta - 0.5\left(1 - \frac{1}{\tan\theta}\right)^2 \sin\theta\tan\theta\right), \tag{53a}$$

when $2 \leqslant \tan\theta < \infty$

$$\frac{\boldsymbol{D}_1}{J\Delta t|\boldsymbol{V}|(\boldsymbol{\Psi}_R-\boldsymbol{\Psi}_L)}=0.25\cos\theta. \tag{53b}$$

(ii) Cell 2:

$$\frac{\boldsymbol{D}_2}{J\Delta t|\boldsymbol{V}|(\boldsymbol{\Psi}_R-\boldsymbol{\Psi}_L)}=0.25\cos\theta\left(\frac{1}{\tan\theta}-1\right). \tag{53c}$$

(iii) Cell 3:
when $1\leqslant\tan\theta<2$

$$\frac{\boldsymbol{D}_3}{J\Delta t|\boldsymbol{V}|(\boldsymbol{\Psi}_R-\boldsymbol{\Psi}_L)}=0.5\left(\sin\theta-\cos\theta-0.5\left(1-\frac{1}{\tan\theta}\right)^2\sin\theta\tan\theta\right), \tag{53d}$$

when $2\leqslant\tan\theta<\infty$

$$\frac{\boldsymbol{D}_3}{J\Delta t|\boldsymbol{V}|(\boldsymbol{\Psi}_R-\boldsymbol{\Psi}_L)}=0.25\cos\theta. \tag{53e}$$

(iv) Cell 4:

$$\frac{\boldsymbol{D}_4}{J\Delta t|\boldsymbol{V}|(\boldsymbol{\Psi}_R-\boldsymbol{\Psi}_L)}=0.25\cos\theta\left(\frac{1}{\tan\theta}-1\right). \tag{53f}$$

Fig. 13 shows the magnitude of $\boldsymbol{D}$ with the newly re-evaluated flux form. It should be noted that unlike the cases of AUSMPW+ and Roe's FDS, the numerical dissipation becomes zero and the initial condition is accepted as the final solution when the angle between discontinuity and cell-interface is 45°. In other words, as multi-dimensional effect becomes stronger, solution becomes more accurate. Thus, the re-evaluated flux is certainly a better flux form for multi-dimensional problems and it is expected to give a significant improvement in solution accuracy. Even for other angles, the total numerical dissipation decreases substantially as in Figs. 12 and 13.

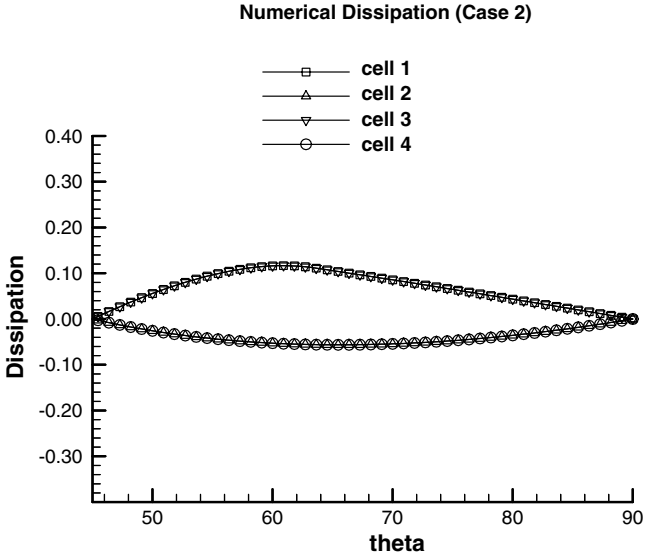

Fig. 13. Numerical dissipation in each cell (case 2).

Case 3: $\boldsymbol{\Psi}_{\frac{1}{2}} = \boldsymbol{\Psi}_{\mathrm{R}}$.

Similar to the previous cases, the flux difference can be summarized as follows:

(i) Cell 1:

$$\frac{\boldsymbol{D}_1}{J\Delta t|\boldsymbol{V}|(\boldsymbol{\Psi}_{\mathrm{R}} - \boldsymbol{\Psi}_{\mathrm{L}})} = -\left(\cos\theta\left(1 - \frac{0.5}{\tan\theta}\right) - 0.5\cos\theta\right). \tag{54a}$$

(ii) Cell 2:

$$\frac{\boldsymbol{D}_2}{J\Delta t|\boldsymbol{V}|(\boldsymbol{\Psi}_{\mathrm{R}} - \boldsymbol{\Psi}_{\mathrm{L}})} = -\cos\theta\left(1 - \frac{0.5}{\tan\theta}\right). \tag{54b}$$

(iii) Cell 3:

when $1 \leqslant \tan\theta < 2$

$$\frac{\boldsymbol{D}_3}{J\Delta t|\boldsymbol{V}|(\boldsymbol{\Psi}_{\mathrm{R}} - \boldsymbol{\Psi}_{\mathrm{L}})} = \sin\theta - \frac{0.5\cos\theta}{\tan\theta} - 0.5\cos\theta - 0.5\left(1 - \frac{1}{\tan\theta}\right)^2 \sin\theta\tan\theta, \tag{54c}$$

when $2 \leqslant \tan\theta < \infty$

$$\frac{\boldsymbol{D}_3}{J\Delta t|\boldsymbol{V}|(\boldsymbol{\Psi}_{\mathrm{R}} - \boldsymbol{\Psi}_{\mathrm{L}})} = \cos\theta\left(1 - \frac{0.5}{\tan\theta}\right). \tag{54d}$$

(iv) Cell 4:

$$\frac{\boldsymbol{D}_4}{J\Delta t|\boldsymbol{V}|(\boldsymbol{\Psi}_{\mathrm{R}} - \boldsymbol{\Psi}_{\mathrm{L}})} = 0.5\cos\theta. \tag{54e}$$

Fig. 14 shows that cell 1 in case 1 and cell 3 in case 3 have the same numerical dissipation, and cell 2 in case 1 and cell 4 in case 3 have the same value. That is, case 1 and case 3 are symmetric and the amount of numerical dissipation is exactly the same.

From the comparative study of flux forms, it is confirmed that case 2 always yields minimal numerical dissipation. Even though the present analysis is carried out when discontinuity is located on grid points as in Fig. 9, the analysis result can be valid in general multi-dimensional situation.

3.1.3. Shock discontinuity

M-AUSMPW+ has the ability to capture stationary shock with only one intermediate cell. Since the convective quantity is determined according to flow condition at a cell-interface, i.e., whether it is subsonic or supersonic, numerical overshoot or oscillation can be avoided completely. Actual computations will be given in Section 4.2.

In case of moving shock discontinuity, it is captured through several intermediate cells. At the head and tail of numerical shock, the ratio of slope variations changes very rapidly and it is almost constant in the middle region (see Fig. 20(b)). Thus, M-AUSMPW+ yields steeper variation than AUSMWP+ throughout the region. As a result, the numerical dissipation of M-AUSMPW+ is reduced and overall accuracy for moving shock case is enhanced again, which is verified in Fig. 20(b).

M-AUSMPW+ becomes identical to AUSMPW+ in case of expansion shock. Thus, it does not admit expansion shock since it chooses the entropy-increasing speed of sound by considering flow direction. The entropy condition of AUSMPW+ is proven in [1].

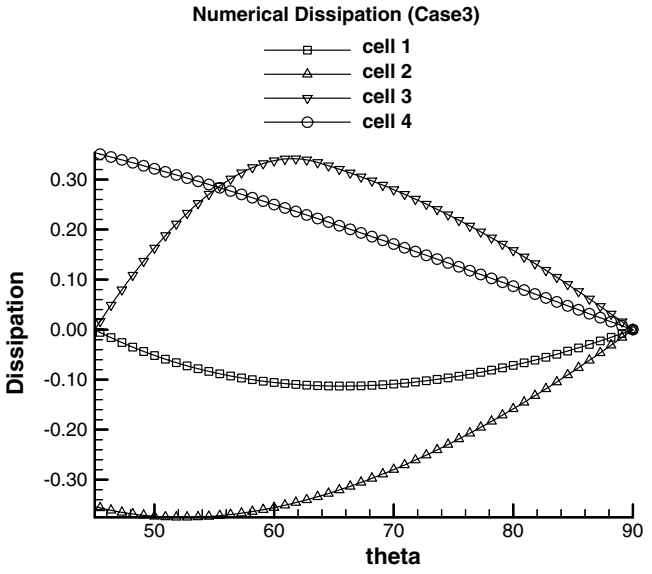

Fig. 14. Numerical dissipation in each cell (case 3).

3.2. Consistency

In order to solve the governing equations correctly, the numerical scheme should satisfy consistency. As Δt and Δx approaches zero and the properties of both cells are equal, numerical flux vector should converge to the physical flux vector of the original governing equations. If $\Delta t, \Delta x \to 0$, $\boldsymbol{\Psi}_{\mathrm{L}} = \boldsymbol{\Psi}_{\mathrm{R}}$ and $\boldsymbol{P}_{\mathrm{L}} = \boldsymbol{P}_{\mathrm{R}}$. Thus, $\boldsymbol{\Psi}_{\frac{1}{2}}$ becomes $\boldsymbol{\Psi}_{\mathrm{L\,or\,R}}$ since $\boldsymbol{\Psi}_{\frac{1}{2}}$ is always between $\boldsymbol{\Psi}_{\mathrm{L}}$ and $\boldsymbol{\Psi}_{\mathrm{R}}$ and the pressure ratio of both cells are equal to unit, which gives $f_{\mathrm{L,R}} = 0$. Then, the split flux vector of M-AUSMPW+ converges to the physical flux vector as follows:

$$\mathbf{F}_{\frac{1}{2}} = \bar{M}_{\mathrm{L}}^{+} c_{\frac{1}{2}} \boldsymbol{\Psi}_{\mathrm{L},\frac{1}{2}} + \bar{M}_{\mathrm{R}}^{-} c_{\frac{1}{2}} \boldsymbol{\Psi}_{\mathrm{R},\frac{1}{2}} + \left(P_{\mathrm{L}}^{+} \boldsymbol{P}_{\mathrm{L}} + P_{\mathrm{R}}^{-} \boldsymbol{P}_{\mathrm{R}}\right) = \left(M_{\mathrm{L}}^{+} + M_{\mathrm{R}}^{-}\right) c_{\frac{1}{2}} \boldsymbol{\Psi}_{\mathrm{L}} + \left(P_{\mathrm{L}}^{+} + P_{\mathrm{R}}^{-}\right) \boldsymbol{P}_{\mathrm{L}} = U\boldsymbol{\Psi} + \boldsymbol{P}. \quad (55)$$

3.3. Efficiency

Table 1a shows the comparison of computational cost for flux function only and Table 1b for overall computational efficiency. Computational time for M-AUSMPW+ includes the time for $\boldsymbol{\Phi}_{\mathrm{superbee}}$ in Eq. (27). For comparison, second order MUSCL approach with van Leer limiter and AF-ADI time integration is employed.

From Table 1a, it is seen that M-AUSMPW+ takes more computational time compared with AUSMPW+ because it includes the routine for $\boldsymbol{\Phi}_{\mathrm{superbee}}$. However, if overall computational cost including time

Table 1a
Comparison of computational cost (flux function only)

Flux function only	M-AUSMPW+	AUSMPW+	AUSM+	Roe's FDS without entropy fix
$\mathrm{Time/time}_{\mathrm{AUSMPW+}}$	1.89	1	0.93	1.35

Table 1b
Comparison of computational cost (overall computation time)

Overall	M-AUSMPW+ van Leer + ADI	AUSMPW+ van Leer + ADI	AUSM+ van Leer + ADI	Roe's FDS without entropy fix van Leer + ADI
$\text{Time/time}_{\text{AUSMPW+}}$	1.10	1	0.99	1.04

integration is taken into account, the ratio reduces to 1.1 in Table 1b. Considering the fact that M-AUSMPW+ provides more than two times grid reduction effect in two-dimensional problems, additional computational cost is very acceptable.

4. Numerical results

4.1. Contact discontinuity

This test case reveals the amount of numerical dissipation when contact discontinuity is inclined to cell-interface. It is closely related to accuracy in pure multi-dimensional phenomena such as vortex flow or separated flow. As known well, AUSM-type schemes or Roe's FDS can give the exact solution in one-dimensional contact discontinuity. Fig. 15 shows the density distribution of a stationary normal contact discontinuity. All of the schemes, including M-AUSMPW+, give the ideal result.

In case of oblique contact discontinuity, it is inevitably smeared due to additional numerical dissipation. Fig. 16 is the result of stationary contact discontinuity inclined to cell-interface by 45° angle. Initial conditions are given as follows:

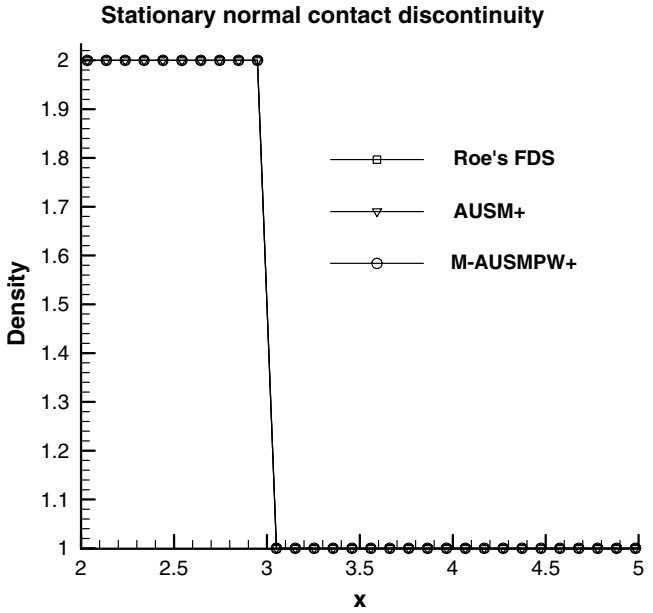

Fig. 15. Stationary normal contact discontinuity according to limiters and numerical schemes.

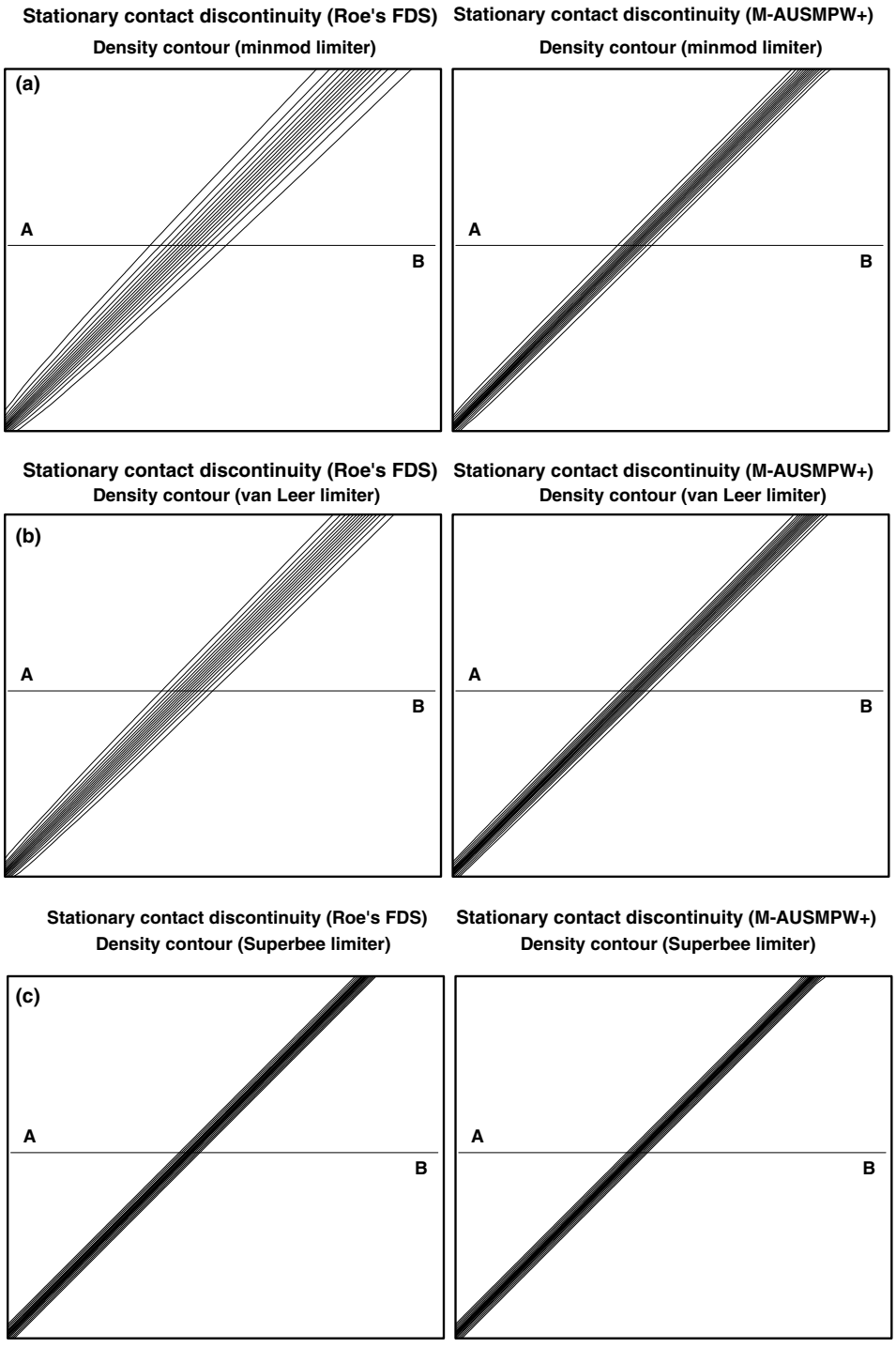

Fig. 16. (a) Comparison of density contours between Roe's FDS and M-AUSMPW+ (minmod limiter). (b) Comparison of density contours between Roe's FDS and M-AUSMPW+ (van Leer limiter). (c) Comparison of density contours between Roe's FDS and M-AUSMPW+ (Superbee limiter).

$$(\rho_L, u_L, v_L, p_L) = (2.0, 0.1, 0.1, 0.714), \quad (\rho_R, u_R, v_R, p_R) = (1.0, 0.1, 0.1, 0.714).$$

The grid system is 60×50. Boundary values along the left end and the bottom are fixed as initial values. Others are extrapolated from the inside. As explained in Section 3.1.2, discontinuity cannot be captured exactly. Once it is smeared, it is not compressed because there is no physical compression mechanism. Thus, the only way to capture contact discontinuity accurately is to minimize numerical dissipation. As in Fig. 16, the computed results become very diffusive compared with normal contact discontinuities. The left and right figures are the density contours of Roe's FDS and M-AUSMPW+ with minmod limiter, van Leer limiter and superbee limiter, respectively. While Roe's FDS with minmod limiter or van Leer limiter gives diffusive results, M-AUSMPW+ captures contact discontinuity almost the same level of Roe's FDS with superbee limiter. Fig. 17 shows density distributions along the line AB in Fig. 16. In case of Roe's FDS, the discontinuity is captured through 13, 9, and 3 cells with minmod, van Leer and superbee limiters. M-AUSMPW+ with the same limiters gives the discontinuity by 4, 4 and 3 cells.

Fig. 18 is the result for moving oblique contact discontinuity inclined to cell-interface by 45° angle. Dual time stepping with AF-ADI is employed for second order temporal accuracy. The results are also sensitive to the amount of numerical dissipation. In case of Roe's FDS, the discontinuity is captured through 13, 9 and 5 cells by minmod, van Leer and superbee limiter. M-AUSMPW+ shows a similar accuracy enhancement as in the case of a stationary contact discontinuity: it is captured through 6, 6 and 5 cells, respectively. This includes additional numerical dissipation by temporal discretization. In conclusion, M-AUSMPW+ shows the almost same results as Roe's FDS with superbee limiter in stationary and moving contact discontinuity, even if minmod or van Leer limiter is used.

Superbee limiter gives the best results in contact discontinuity. But it cannot be used in continuous region, which will be mentioned in Section 4.4. In this respect, M-AUSMPW+ is very promising. M-AUSMPW+ can be used both in continuous and discontinuous regions: it can capture contact discontinuity at the same accuracy level of superbee limiter, and simultaneously, it gives a significant accuracy enhancement in continuous region.

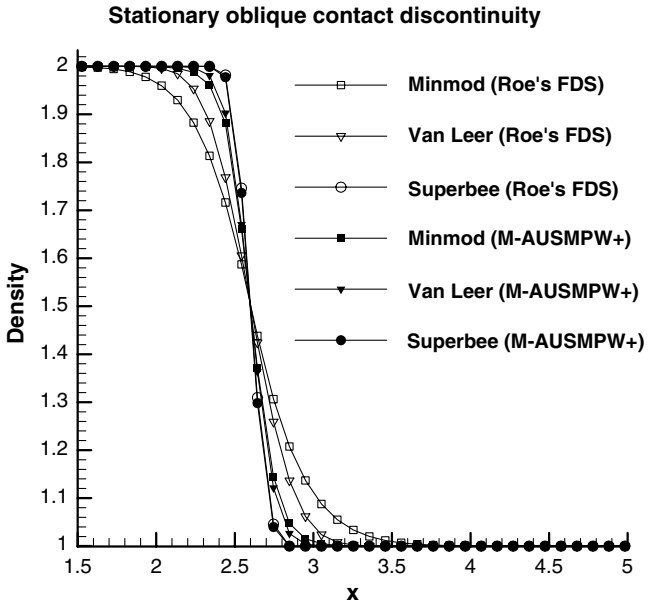

Fig. 17. Stationary oblique contact discontinuity according to limiters and numerical schemes.

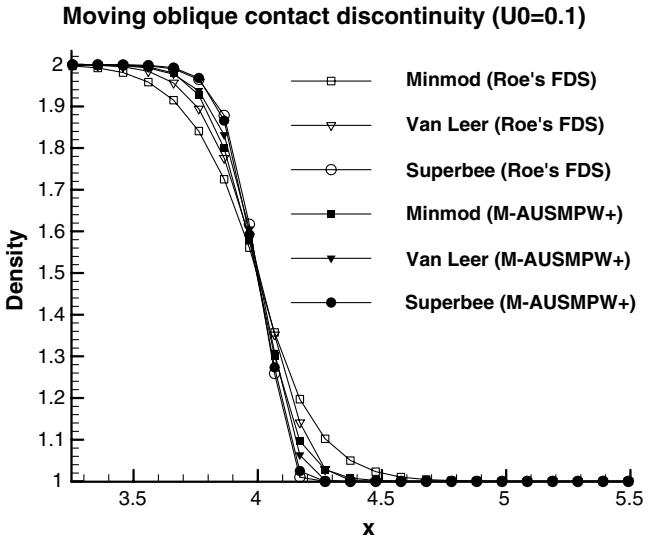

Fig. 18. Moving oblique contact discontinuity according to limiters and numerical schemes.

4.2. Shock discontinuity

This test is performed to investigate the stationary shock-capturing characteristic of M-AUSMPW+ according to the relation between sonic transition position and cell-interface. From the Prandtl relation, the value of $M_{i+\frac{1}{2}} = M_1^* M_2^*$ is one. Thus, if the value of $M_{i+\frac{1}{2}} = M_i^* M_{i+1}^*$ is one at a cell-interface, the location of the cell-interface is exactly the same as shock position. For that reason, $M_{i+\frac{1}{2}} = M_i^* M_{i+1}^*$ can be the good indicator to express shock position. $M_{i+\frac{1}{2}} = M_i^* M_{i+1}^* > 1$ means that the cell- interface is in supersonic region and $M_{i+\frac{1}{2}} = M_i^* M_{i+1}^* < 1$ means that the cell-interface is in subsonic region (see Fig. 5) [13].

The initial conditions for a stationary shock wave are as follows:

When $M_1 > 1 > M_2$:

Case (a): $M_{i-1} = M_i = M_1,\ M_{i+1} = M_2$.
Case (b): $M_{i-1} = M_1,\ M_i = 0.5(M_1 + 1) > 1,\ M_{i+1} = M_2$.
Case (c): $M_{i-1} = M_1,\ M_i = 0.5(M_2 + 1) < 1,\ M_{i+1} = M_2$.
Case (d): $M_{i-1} = M_1,\ M_i = M_{i+1} = M_2$.

In case of (b), $M_{i+\frac{1}{2}} = M_i^* M_{i+1}^* < 1$, thus, the modified pressure splitting function of Eq. (39) is turned on. Fig. 19 shows the final computed solutions. Computations are converged to machine accuracy zero. It shows that M-AUSMPW+ has the ability to capture monotonic shock profile with only one intermediate cell in stationary shock discontinuity, regardless of sonic transition position. Although, the convective quantity is modified, M-AUSMPW+ does not show numerical overshoots or oscillations. This is because the convective quantity is designed to satisfy the monotonic constraint of r2 and to recognize whether cell-interface is located at subsonic or supersonic region as in Eq. (39). Fig. 20 is the results for moving shock discontinuity. Shock strength is equivalent to the 45° stationary oblique shock with the Mach number of 2, and it is moving into stationary region. For time integration, second order dual-time stepping method is used. Fig. 20(a) is pressure distributions along the x-direction. Computations with minmod and van Leer limiter yield reasonable solutions. In case of superbee limiter, pressure wiggle is observed in post-shock

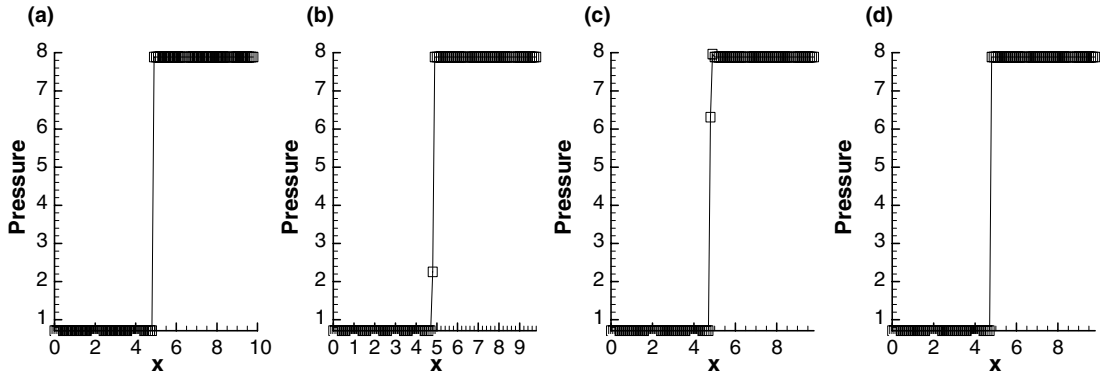

Fig. 19. Stationary shock discontinuity according to the location of sonic transition position.

region. Fig. 20(b) shows the magnified pressure distribution around shock region. M-AUSMPW+ is monotonic as well as more accurate compared to Roe's FDS. Also, it is observed in Fig. 20 that the modification of $P^{\pm}_{\mathrm{L,R}}$ does not cause any problem even for unsteady shock wave.

4.3. Rarefaction wave

Initial conditions are given as follows:

$$(\rho, u, p)_{\mathrm{L}} = (3, 0.9, 3), \quad (\rho, u, p)_{\mathrm{R}} = (1, 0.9.1).$$

Fig. 21 is the results of 1st order Roe's FDS without entropy fix, AUSMPW+ and M-AUSMPW+ with $\Delta x = 0.2$ and a grid number of 200. Non-dimensionalized time is 10 and 3rd order TVD Runge–Kutta time integration scheme [9] is used. CFL number is 0.5. As known well, Roe's FDS without entropy fix shows expansion shock in a rarefaction region. On the other hand, AUSMPW+ or M-AUSMPW+ does not yield such problem because the speed of sound in M-AUSMPW+, like AUSMPW+[1], possesses the ability to distinguish expansion shock wave from compression shock wave (see Fig. 22).

4.4. Stationary vortex flow

Vortex flow is characterized by the existence of negative pressure gradient toward core and curved streamlines. Thus, it can be regarded as a pure multi-dimensional phenomenon, and in most applications, it is very difficult or impossible that the flow is aligned with grid system. Moreover, in core region where pressure gradient changes very steeply, computed results are smeared very much.

Vortex model is Thomson–Rankine vortex model which is composed of free vortex outside the core and forced vortex inside the core.

(a) Free vortex (outside the core)

$$V_\theta \cdot r = \text{constant} \quad \text{and} \quad \frac{1}{\rho}\frac{\partial p}{\partial r} = \frac{V_\theta^2}{r}. \tag{56a}$$

(b) Forced vortex (inside the core)

$$V_\theta = \omega \cdot r \quad \text{and} \quad \frac{\mathrm{d}p}{\mathrm{d}r} = \rho\frac{V_\theta^2}{r}. \tag{56b}$$

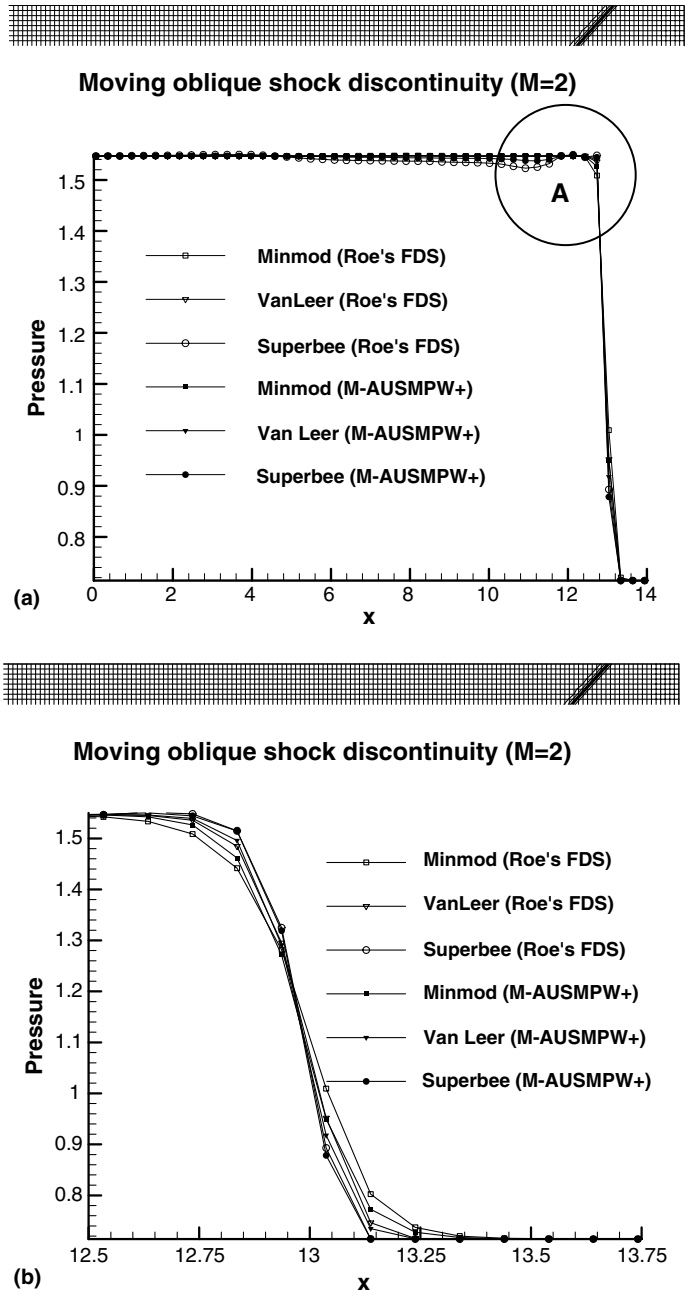

Fig. 20. (a) Comparison of pressure distribution of fast moving oblique shock discontinuity. (b) Comparison of magnified pressure distribution.

Angular velocity ω is 3, core radius is 0.2 and maximum velocity is $0.54c_\infty$. Total computational domain is from -2 to 2 with equal spacing. For grid convergence test, 25×25, 50×50, 75×75 and 100×100 grid points are selected. Roe's FDS, AUSMPW+ and M-AUSMPW+ are used for numerical fluxes. 3rd Order

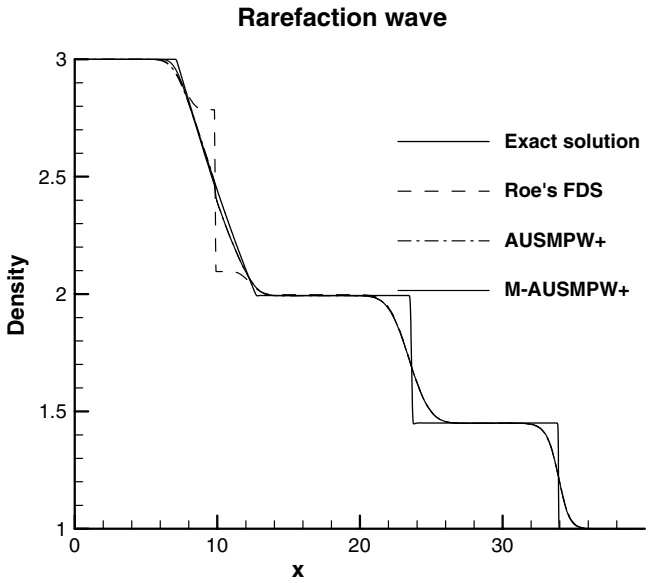

Fig. 21. Density distribution of rarefaction wave.

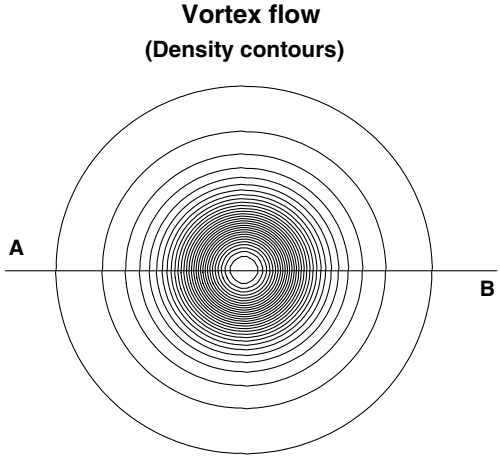

Fig. 22. Density contour for a vortex flow.

TVD Runge–Kutta time integration is used and CFL number is 0.8. Boundary conditions are fixed as initial values. Pressure distribution is plotted at the non-dimensionalized time of 40.

Fig. 23 shows density distributions according to numerical fluxes, plotted along the line AB. Fig. 23(a) is the result of minmod limiter. Roe's FDS and AUSMPW+ results are somewhat diffusive but M-AUSMPW+ provides much more improved result. Compared to the result by AUSMPW+ on four times denser grid system, M-AUSMPW+ is about twice more accurate. A similar tendency in accuracy improvement can be observed when van Leer limiter is used.

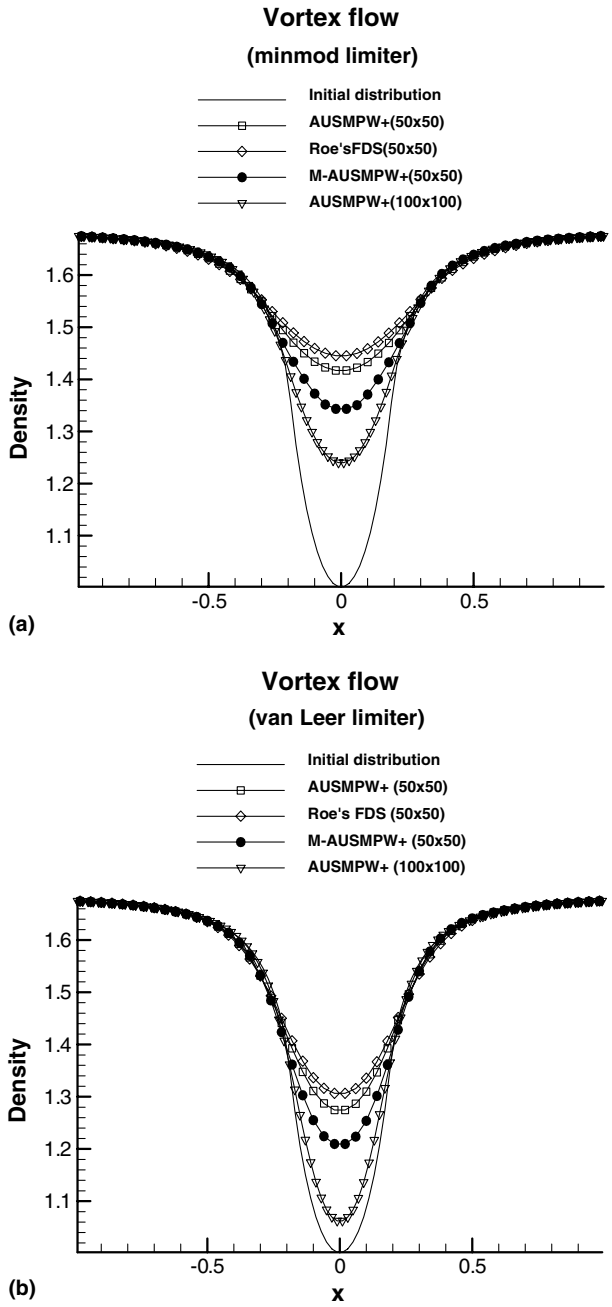

Fig. 23. (a) Comparison of density distribution along the line AB (minmod limiter). (b) Comparison of density distribution along the line AB (van Leer limiter).

Fig. 24 is the comparison of entropy variation and Fig. 25 is the characteristics of grid convergence. As expected, entropy increase is minimal in case of M-AUSMPW+. M-AUSMPW+ with van Leer limiter is asymptotically close to the result by AUSMPW+ with 3rd order interpolation without any limiting

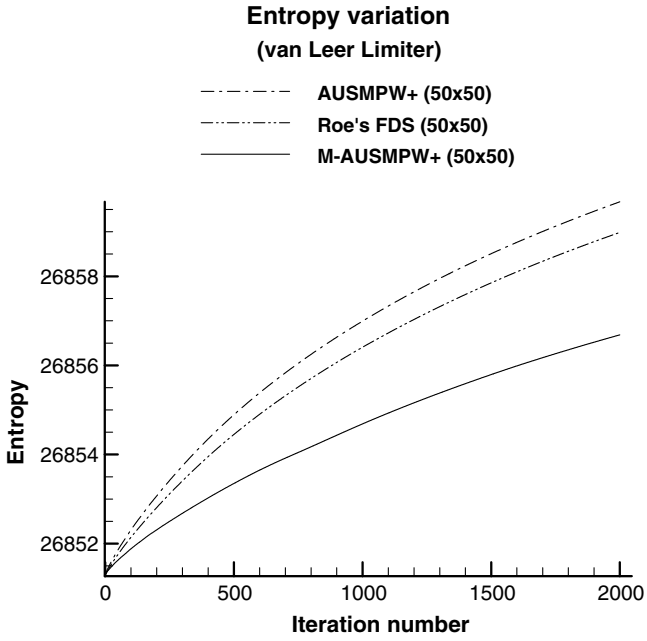

Fig. 24. Comparison of entropy variation (van Leer limiter).

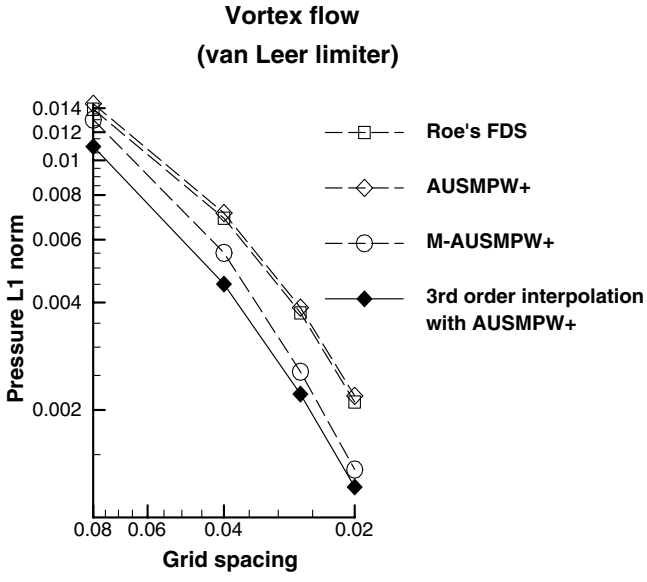

Fig. 25. Comparison of grid convergence test according to flux functions (van Leer limiter).

function. The result of superbee limiter is not included, because vortex strength is artificially amplified as computation continues, i.e., entropy is decreasing continuously and finally computation fails. Thus, superbee limiter cannot be used for this type of flows, even though it gives the best results in a contact or a slip

discontinuity. Aside from the reason, it has monotonicity and convergence problems in multi-dimensional flows. In this respect, M-AUSMPW+ can be one of the best choices for multi-dimensional flows without compromising the accuracy in a contact or slip discontinuity.

4.5. Shock wave/ boundary-layer interaction

The shock wave/boundary-layer interaction problem has been widely used for a viscous flow validation. The free stream Mach number is 2 and the shock impinging angle is 32.5°. Reynolds number is 2.96×10^5. The grid system is 56×59 and the denser grid is 150×200. It is known as a steady problem and AF-ADI is used for temporal integration. Fig. 26 shows the comparison of pressure contours between Roe's FDS and M-AUSMPW+ with van Leer limiter. Fig. 27 is the pressure distribution along the line AB. The flow structure by M-AUSMPW+ presents expansion and re-compression waves more clearly because separated flow is resolved more accurately. Fig. 28 shows the comparison of skin friction coefficients. Since separated flow is not aligned with grid lines, a scheme should capture oblique contact discontinuity accurately for the accurate calculation of separation region. From the numerical test of oblique contact discontinuity in Section 4.1, M-AUSMPW+ is expected to improve accuracy significantly in this region. It is certified by Figs. 28(a) and (b). Separation region by M-AUSMPW+ is closer to the result on denser grid system. Fig. 28(c) and Table 2 show the comparison of area ratio in separation region.

Separation region by Roe's FDS with minmod limiter is very narrow but the same computation by M-AUSMPW+ is similar to Roe's FDS with van Leer limiter. Also, M-AUSMPW+ with van Leer limiter

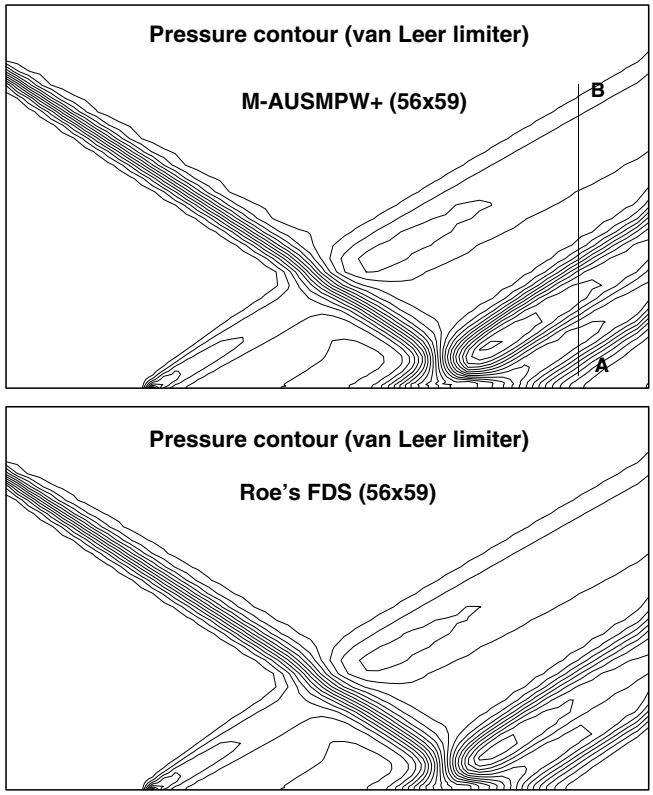

Fig. 26. Comparison of pressure contours (van Leer limiter).

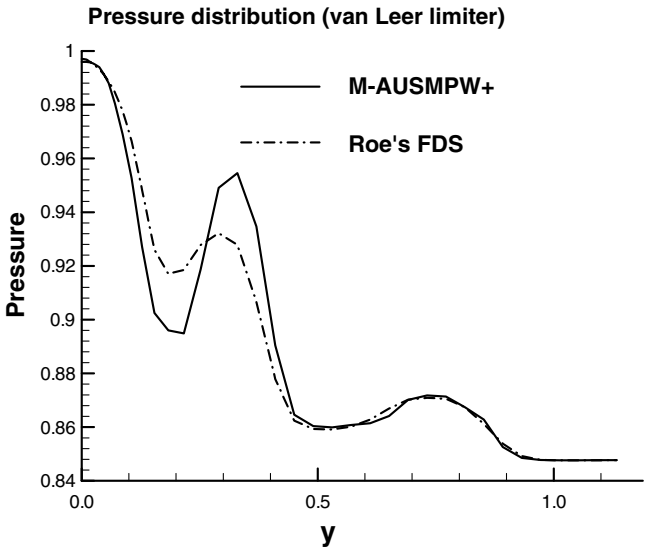

Fig. 27. Comparison of pressure distribution along the line AB (van Leer limiter).

shows a significant accuracy enhancement and separation region is very close to the result on denser grid system. Fig. 29 shows the error history of M-AUSMPW+. Convergence characteristic is similar to Roe's FDS or AUSMPW+.

4.6. Viscous shock tube problem

This test problem was studied by Daru and Tenaud [17] and Sjögreen and Yee [18]. It is a shock tube problem in 2-D square box with unit length, $0 \leqslant x,y < 1$, and the diaphragm is located at $x = 0.5$. The initial state is given as follows:

$$(\rho, u, v, p)_{\mathrm{L}} = (120, 0, 0, 120/\gamma) \quad \text{and} \quad (\rho, u, v, p)_{\mathrm{R}} = (1.2, 0, 0, 1.2/\gamma).$$

The Reynolds number is 200 and the viscosity is constant. For the fair comparison of AUSMPW+ and M-AUSMPW+, the viscous flux terms of the governing equations are calculated by 4th order interpolation.

At $t = 0$, diaphragm is broken and the shock wave moves toward $x = 1$. Then, it is reflected and complex flow interactions occur. 3rd order TVD Runge–Kutta time integration is used and the results are at non-dimensionalized time of 1. CFL number is 0.5. Fig. 30(a) is the comparison of the density contour of AUSMPW+ and M-AUSMPW+ with van Leer limiter. The grid size is 250×125. Fig. 30(b) is the results on 500×250 grid system. After the interaction between boundary layer and the lambda shock, vortices due to flow separation are generated and they grow up on the downstream side. From [18], the results with 500×250 grid system is very similar to the grid converged solution, which will be validated again in Part II. Due to the effect of numerical dissipation in multi-dimensional flows, the growth of the primary vortex by AUSMPW+ in Fig. 30(a) is relatively slower and it is less rotated compared with the results of M-AUSMPW+. Fig. 31(a) shows that more clearly. The nearest solution to the grid converged solution is the result of M-AUSMPW+ on 500×250 grid system. AUSMPW+ is certainly much more diffusive than M-AUSMPW+ on 250×125 grid system. Fig. 31(b) shows that the result of M-AUSMPW+ by 250×125 (=31,250) grids is almost the same with AUSMPW+ by 350×175 (=61,250) grids. Table 3 is the

Table 2
Comparison of the area ratio of separation region

Scheme	Roe's FDS (van Leer limiter) (150×200)	M-AUSMPW+ (van Leer limiter) (56×59)	M-AUSMPW+ (minmod limiter) (56×59)	Roe's FDS (van Leer limiter) (56×59)	Roe's FDS (minmod limiter) (56×59)
Area ratio	1	0.912	0.539	0.600	0.220

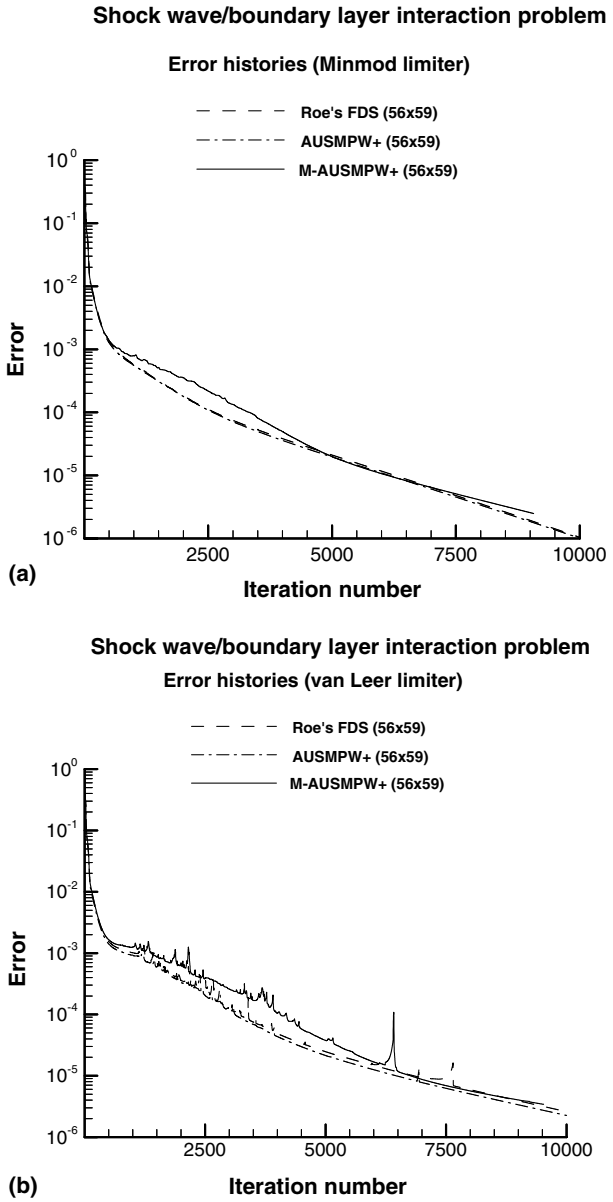

Fig. 29. (a) Comparison of convergence (minmod limiter). (b) Comparison of convergence (van Leer limiter).

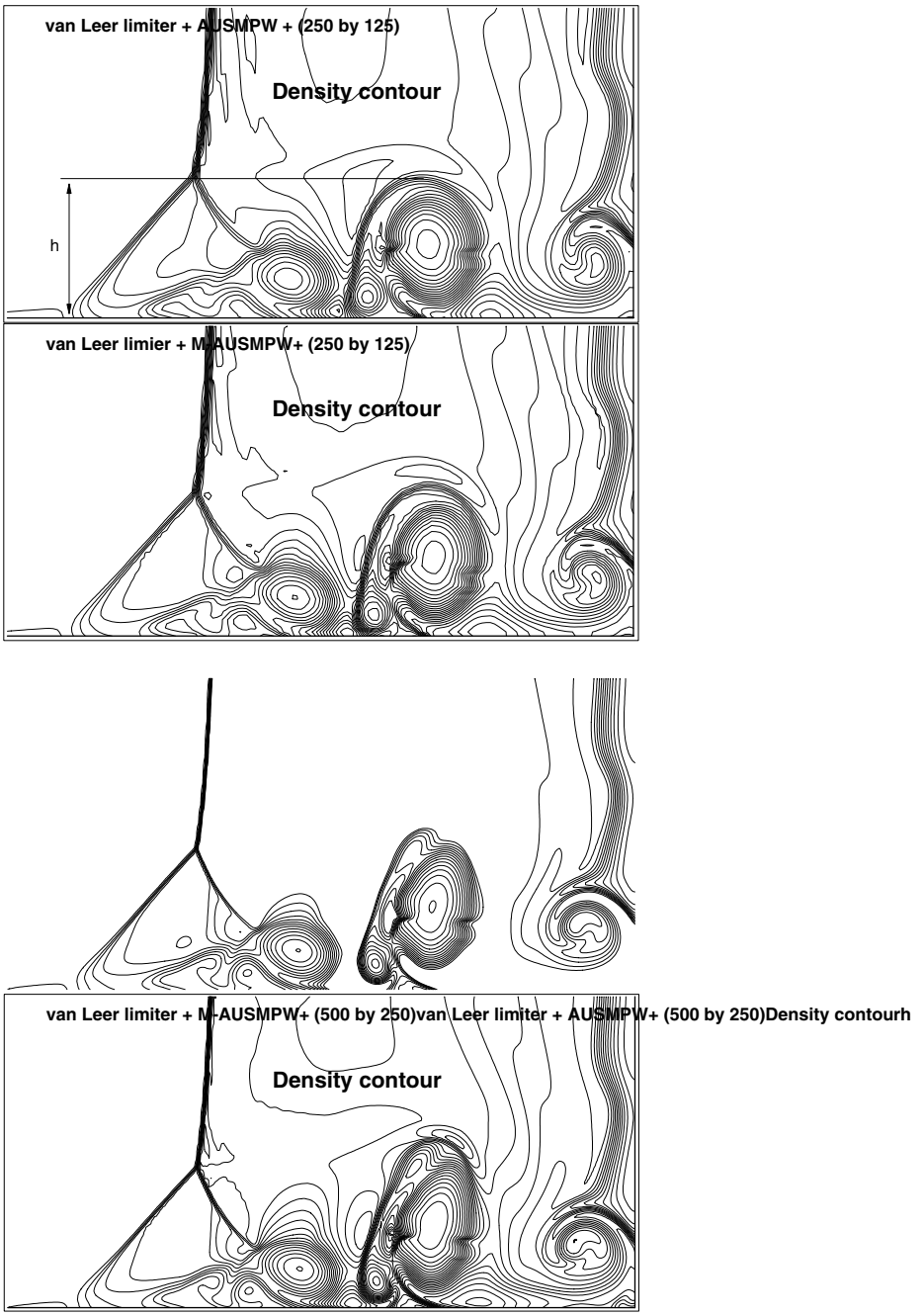

tions. By implementing M-AUSMPW+ in three-dimensional computations, the accuracy improvement is expected to be more visible: M-AUSMPW+ can present the grid reduction effect to $2^{-\frac{3}{2}}$ in three-dimensional computations.

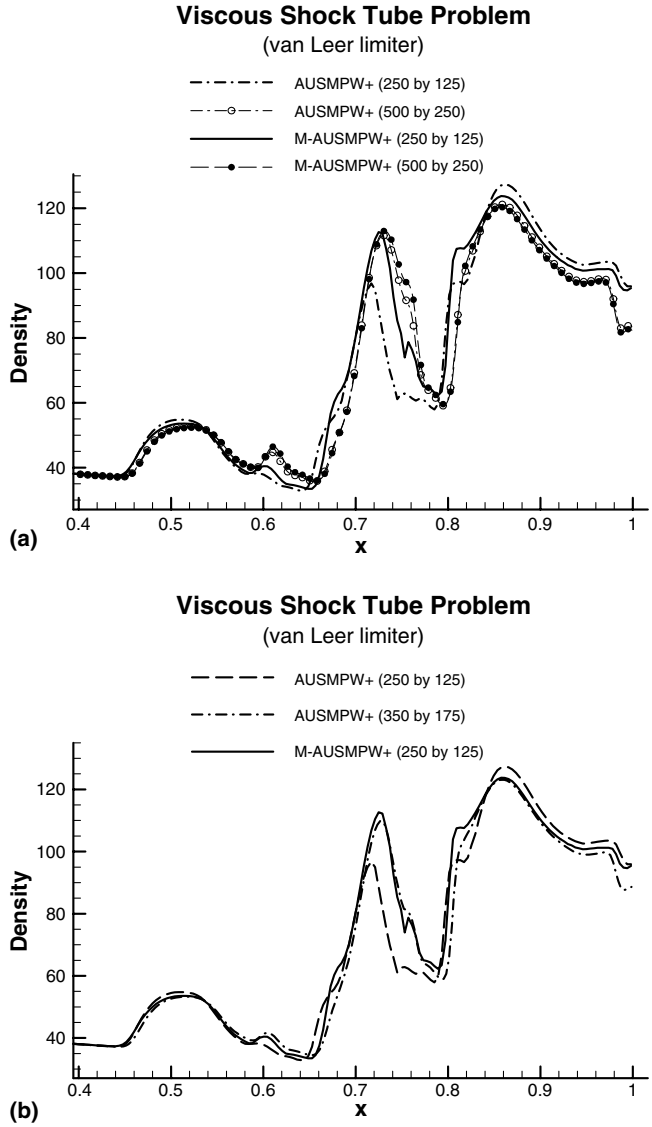

Fig. 31. (a) Comparison of density distribution along the wall. (b) Comparison of density distribution along the wall.

Table 3
Comparison of the height of primary vortex

Scheme	AUSMPW+ (van Leer limiter) (250×125)	M-AUSMPW+ (van Leer limiter) (250×125)	AUSMPW+ (van Leer limiter) (350×175)	AUSMPW+ (van Leer limiter) (500×250)	M-AUSMPW+ (van Leer limiter) (500×250)
Height (h)	0.142	0.154	0.155	0.163	0.166

5. Conclusions

A new treatment of a cell-interface convective flux which typically appears in AUSM-type methods is introduced to substantially reduce numerical dissipation in smooth region without compromising accuracy in shock region. The core idea of the new method is to modify the convective quantity at a cell-interface by considering flow physics. Through the analysis of TVD limiters, a simple criterion to predict a more accurate cell-interface state is proposed and the convective quantity is re-evaluated according to the criterion. The practical advantages of the proposed method can be revealed in two aspects. One is that the newly defined cell-interface value is closer to the real physical value. The other is that it can eliminate numerical dissipation effectively in non-flow aligned grid system. Thus, M-AUSMPW+, a new scheme formulated by incorporating the re-evaluation procedure, improves solution accuracy significantly in multi-dimensional problems.

Another desirable characteristic of M-AUSMPW+ is monotonicity in capturing a steady shock wave, regardless of the location of sonic transition position. As a result, convergence characteristics and grid dependency of AUSM-type methods are remarkably enhanced.

Through numerous test cases such as stationary and moving physical discontinuities, rarefaction wave, vortex flow, shock wave/boundary-layer interaction, and viscous shock tube problem, M-AUSMPW+ is proved to be equally efficient but about twice more accurate than previous schemes. If M-AUSMPW+ would be applied to three-dimensional problems, accuracy and efficiency is expected to be improved further.

Acknowledgments

The authors appropriate the financial support by Agency for Defense Development (ADD) and by the Brain Korea-21 Program for the Mechanical and Aerospace Engineering at Seoul National University. We give the special thank to Dr. Sungsoo Kim for the help of revising the present paper. We appreciate referees for critical comments and valuable suggestions.

References

[1] K.H. Kim, C. Kim, O.H. Rho, Methods for the accurate computations of hypersonic flows, Part I: AUSMPW+ scheme, J. Comput. Phys. 174 (2001) 38–80.
[2] P.L. Roe, Discrete models for the numerical analysis of time-dependent multidimensional gas dynamics, J. Comput. Phys. 63 (1986) 458–476.
[3] M.S. Liou, A sequel to AUSM: AUSM+, J. Comput. Phys. 129 (1996) 364–382.
[4] A. Harten, High resolution schemes for hyperbolic conservation laws, J. Comput. Phys. 49 (3) (1983) 357–393.
[5] P.K. Sweby, High resolution schemes using flux limiters for hyperbolic conservation laws, SIAM J. Numer. Anal. 21 (5) (1984) 995–1011.
[6] C. HirshNumerical Computation of Internal and External Flows, vol. 1.2, Wiley, Berlin, 1990.
[7] A. Harten, B. Enquist, S. Osher, S.R. Chakravarthy, Uniformly high order accurate essentially non-oscillatory schemes, III, J. Comput. Phys. 71 (2) (1987) 231–303.
[8] A. Harten, S. Osher, Uniformly high order accurate non-oscillatory schemes I, SIAM J. Numer. Anal. 24 (1987) 279–309.
[9] C.W. Shu, S. Osher, Efficient implementation of essentially non-oscillatory shock-capturing schemes, J. Comput. Phys. 77 (1988) 439–471.
[10] D. Pan, S.C. Lee, A fixed-stencil non-oscillatory scheme for hyperbolic systems, J. Comput. Phys. 100 (1992) 200–204.
[11] X-D. Liu, S. Osher, T. Chan, Weighted essentially non-oscillatory schemes, J. Comput. Phys. 115 (1994) 200–212.
[12] G.S. Jiang, C.W. Shu, Efficient implementation of weighted ENO schemes, J. Comput. Phys. 126 (1996) 202–228.
[13] K.H. Kim, C. Kim, O.H. Rho, A Study on the Monotonic Characteristic of AUSM-type Schemes in Shock Regions, ICAS, Toronto, 2002, September.

[14] C.W. Shu, TVB uniformly high-order schemes for conservation laws, Math. Comput. 49 (179) (1987) 105–121.
[15] A. Suresh, H.T. Huynh, Accurate monotonicity-preserving schemes with Runge–Kutta time stepping, J. Comput. Phys. 136 (1997) 83–99.
[16] G. Billet, O. Louedin, Adaptive limiters for improving the accuracy of the MUSCL approach for unsteady flows, J. Comput. Phys. 170 (2001) 161–183.
[17] V. Daru, C. Tenaud, Evaluation of TVD high resolution schemes for unsteady viscous shocked flows, Comp. Fluids 30 (2001) 89–113.
[18] B. Sjögreen, H.C. Yee, Grid convergence of high order methods for multiscale complex unsteady viscous compressible flows, J. Comput. Phys. 185 (2003) 1–26.